ISSN 0915-633X

NATIONAL INSTITUTE FOR FUSION SCIENCE

Development of an Imaging VUV Monochromator in Normal Incidence Region

Joong-San Koog

(Received - June 26, 1996)

NIFS-423 July 1996

RESEARCH REPORT
NIFS Series

NAGOYA, JAPAN

Development of an Imaging VUV Monochromator in Normal Incidence Region

Joong-San Koog

Department of Fusion Science

The Graduate University for Advanced Studies

Abstract

In high temperature laboratory plasmas used for fusion research, there are considerable spatial variations of plasma parameters from the central part to the plasma edge. Spectroscopic diagnoses in the vacuum ultraviolet (VUV) region, therefore, require instruments which provide spatially resolved measurements for accurate determination of radiative power losses and impurity concentrations. Especially, the spatial distributions of different impurity ions are useful for understanding the impurity transport and confinement properties. In non-axisymmetric plasmas or plasmas with complicated spatial structure, two-dimensional image measurement like human eyes' observation may be attractive. For this purpose, we have developed a two-dimensional imaging monochromator system in VUV wavelength region from 400 to 2000Å.

The imaging is achieved with utilizing the pinhole camera effect created by an entrance slit of limited height. The point is that for near normal incidence, the sagittal focusing (perpendicular to the dispersion plane) of a diffracted light by a spherical concave grating is produced at the point outside the Rowland circle. Then, by displacing a two-dimensional detector away from the sagittal focusing point, a one-to-one correspondence between the position of a point on the detector and where it originated in the source is accomplished. The important features of this scheme are two-dimensional imaging which does not require a stigmatic property for focusing and easy fabrication with minor modifications of a commercial normal incidence monochromator.

A 1-m normal incidence monochromator with off-Rowland circle mounting is used for this imaging system. The equipped spherical concave grating has the ruling of 1200-lines/mm and is blazed at 1500 Å. The detector system consists of two subsystems: a two stages microchannel plate image intensifier assembly and a charge coupled device camera.

Ray tracing has been performed to evaluate the imaging properties in the practical geometric configuration and to determine the detector position. The focusing property perpendicular to the dispersion plane was verified by the simple experiment using Hg source and photographic film and compared to the result of ray-tracing.

In order to measure the spatial resolution and the relative sensitivity on spatial coverage of the imaging system, a stationary arc discharge (TPD-S) was developed as a light source. In order to measure the spatial resolution of the imaging system, an aperture mask has been settled to the position of 40 cm in front of the entrance slit. The measured spatial resolution is about 0.5 mrad and 1 mrad in the dispersion and vertical plane, respectively, with the entrance slit of 0.1 mm width and height. The spatial sensitivity was also tested using a mercury lamp or the TPD-S apparatus for the VUV wavelength region. The flat sensitivity was concluded in the direction perpendicular to the dispersion plane. However, it is found that there is a strong non-uniformity of the sensitivity in the direction of the dispersion plane, depending on the observed wavelengths and the blazed wavelength of the used grating. This strong variation in horizontal sensitivity is recognized as the effect of a grating.

The usefulness of the imaging system was demonstrated by applying to the experiment of JIPP T-IIU tokamak plasma. The measured distribution of C IV emission at 1548.2 Å shows that C IV ion is concentrated in the radial position of ~20 cm (The limiter radius is ~23 cm) and spreads uniformly in the toroidal direction. The differences of the radial distributions which depend on ion species and their ionization stages have been observed on the emission lines of Li-like impurity C IV 1548.2 Å, N V 1238.8 Å and O VI 1031.9 Å. Temporal behaviors of the radial distribution have been also measured for O VI emission line at 1031.9 Å.

We have analyzed and tested the system of imaging monochromator based on pin-hole techniques. The optical characteristics of the system appear promising. In principle, the non-uniformity problem of the sensitivity in the dispersion plane may be solved with an introduction of a non-blazed holographic grating. The interchangeable grating mount equipped with several gratings with different blazed wavelengths is thought to be useful in practice. By incorporating a multilayer coated grating, which can produce high reflectivity at non-grazing angles as Bragg reflectors, the imaging system shown here will be applicable even in the extreme-ultraviolet and soft x-ray region.

Key words : imaging monochromator, vuv spectroscopy, ray-tracing tokamak, impurity transport

Acknowledgments

Special thanks go to Prof. Kuninori Sato, my thesis adviser, for his continuous encouragements, valuable discussions, and a great deal of advice and assistance in preparing this manuscript.

I would like to thank Prof. K. Toi, Prof. K. Adati, Dr. T. Seki for their useful discussions and support in running the JIPP T-IIU tokamak. Thanks are due to Prof. J. Fujita and Prof. Y. Hamada for their continuing encouragement. I cannot complete this work without thanking numbers of people in National Institute for Fusion Science (NIFS). I wish to express my gratitude to all of these people.

I thank Prof. J. L. Schwob and Prof. M. Finkenthal from the Racah Institute of Physics at the Hebrew University of Jerusalem for their useful comments. Y. Kondo and members of his class from the Daido Institute of Technology are also acknowledged for producing the test plasma source.

I also wish to express my gratitude to Prof. T. N. Lee and Prof. D. Kim at Pohang University of Science and Technology for their encouragement. I am also grateful to many friends in POSTECH. Dr. S. J. Youn is to be thanked for introducing the Fortran code.

I wish to thank many friends, Masaki Osakabe, Hajime Sakakita, Akira Tanike, Hideharu Kuramoto, Mitsutake Isobe, R. Pavlichenko and H. Takayama, in NIFS for their heartful kindness and their help. I am

also grateful to my countrymen. Fellowship and friendship with them have enriched my life here in Nagoya and made me grow spiritually during the past 3 year. Thanks also go to the numbers of Tsushima rotary club and counselers; Y. Takumi and K. Inagaki.

I would like to express special gratitude to my parents, brothers, and relatives.

Table of Contents

1. Introduction

1.1 Spectroscopic VUV Diagnostics

Spectroscopic diagnostics in the vacuum ultraviolet (VUV) region have been extensively studied for measuring radiation losses, impurity concentrations, impurity transport and atomic processes of highly ionized ions in the magnetically confined high temperature plasmas.

VUV diagnoses in fusion research require instruments which provide a spatially resolved measurement for accurate determination of radiative power losses and impurity concentrations. Especially, the spatial distributions of the different impurity ions are useful for understanding the impurity transport and confinement properties.

1.2 Review of the Space-Resolved Measurements

Various types of instruments for the space resolved measurements have been developed for VUV diagnostics in magnetically confined plasmas.

A duochromator with gold-coated tilting mirror placed in front of the entrance slit has been used in tokamak plasmas, which allows a number of spatial scans to be made in a single shot.[1, 2]

By utilizing the astigmatism of a grazing incidence concave grating, the multispectral spectrograph which has a space resolution has been developed.[3, 4]

With the same principle as above spectrograph, the grazing-incidence spectrograph equipped with a flat-field aberration-corrected concave grating has been used to measure the spatial distribution of VUV radiation in tandem mirror plasma.[5]

1.3 Overview

For the plasma with axis-symmetry, the radial distributions of radiation are important features. In this case, spatial-resolved measurements in the radial direction are interested.[6]

On the contrary, in non-axisymmetric plasmas or plasmas with complicated structure, two-dimensional image measurement like human eyes' observation may be attractive.

This paper describes a development of the two-dimensional imaging monochromator system.

A commercial normal incidence monochromator working on off-Rowland circle mounting[7] is used for this purpose. The imaging is achieved with utilizing the pinhole camera effect created by an entrance slit of limited height. The astigmatism in the normal incidence mounting is small compared with a grazing incidence mount, but has a finite value. The point is that for near normal incidence, the vertical focusing with a concave grating is produced at outside across the exit slit.

Therefore, by putting a 2-D detector at the position away from the exit slit (~30 cm), a one-to-one correspondence between the position of a point on the detector and where it originated in the source is accomplished.

The principle and development of the imaging monochromator using the off-Rowland mounting, including the 2-D detector system are described in chapter 2. A computer simulation by ray tracing for investigations of the imaging properties of the imaging system, and aberration from the spherical concave grating on the exit slit are discussed in chapter 3. The plasma light source (TPD-S) for the test experiments is described in chapter 4. Performances of the imaging monochromator system on the spatial resolution and sensitivity are presented in chapter 5. In chapter 6, the use of this system for diagnostic studies on the JIPP T-IIU tokamak is covered briefly.

2. Imaging Monochromator

2.1 Basic Concept of an Imaging Monochromator

A) Vertical Focusing Property of a Spherical Concave Grating.

Here, the focusing property in vertical direction of a spectrometer is discussed in connection with an imaging.

In order to avoid confusions related to the designation of directions and locations, we take the coordinate attached to a grating. Then, we call the direction parallel to the dispersion plane of the grating as horizontal (meridional). And the direction perpendicular to the dispersion plane is called as vertical (sagittal). In other words, horizontal is a direction perpendicular to the grating rulings, and vertical is a direction parallel to the grating rulings.

According to Fermat's principle of least time, the best horizontal focal point for the spherical concave grating is given by

$$\frac{\cos^2\alpha}{r} - \frac{\cos\alpha}{R} + \frac{\cos^2\beta}{r'} - \frac{\cos\beta}{R} = 0 \qquad (2-1)$$

where α and β are the angles of incidence and diffraction, respectively. R is a radius of curvature of the grating. r and r' are the distances from the grating center to the entrance slit and the exit slit, respectively.

Astigmatism Δz is approximately given by

$$\Delta z \approx r' L \left(\frac{1}{r} + \frac{1}{r'} - \frac{\cos\alpha + \cos\beta}{R} \right) \qquad (2-2)$$

where L is the z-axis value of a point on the grating where the incidence ray is diffracted..

As shown in eq. (2-2), astigmatism has a finite value even in near normal incidence mounting.

In the field of astrophysical research associated with a use of telescope, stigmatic focusing is required for the transfer of an image on the entrance slit into an image on the exit slit. This stigmatism which image a point on the entrance slit or on the object into a point on the exit slit has been achieved with a concave toroidal grating in near normal incidence[8] or a toroidal mirror as a focusing element for a spherical grating in the grazing incidence region[9].

The above imaging spectrometers based on the stigmatic property enable us the spatially resolved measurements along the vertical direction.

Though, when we take pin-hole techniques in the configuration for spatially resolving spectrometer, stigmatic properties are not always necessary. Especially, for the monochromated imaging like human eye's observation, a vertical focusing away from the exit slit position is necessary. In the case of mounting equipped with a spherical concave grating, the vertical focusing of diffracted light is possible within the range of near normal incidence.

B) Principle of an Imaging Monochromator System

A schematic diagram of the optical system is shown in Fig. 2-1. The system uses a spherical concave grating, an entrance slit of limited height, an exit slit and a planar detector. As in the case of a spherical concave mirror, the concave grating in near normal incidence will image a point source first into a vertical line (horizontal focus), then into a horizontal line (vertical focus).

In the horizontal plane, the rays emitted from points of a plasma source pass through the entrance slit, strike the grating, are dispersed and focused on the exit slit. Then the focused rays diverge again, and fall on points on the detector. Optical diagram in the horizontal plane is shown in Fig. 2-1(b). It shows that the rays from points A and B in the plasma fall on points A' and B', respectively.

Similarly, the rays emitted in the vertical plane are traced through, but focused at outside across the exit slit, which is depend on the wavelength. In the case of the near normal incidence, vertical focal point r' for the diffracted image is given from the eq. (2-2) as

$$\frac{1}{r} - \frac{\cos\alpha}{R} + \frac{1}{r'} - \frac{\cos\beta}{R} \approx 0 \qquad (2-3)$$

Fig. 2-1(c) shows that the rays from points C and D fall on points C' and D', respectively.

Therefore, by putting a 2-D detector at the position away from the exit slit of the monochromator, a one-to-one correspondence between the

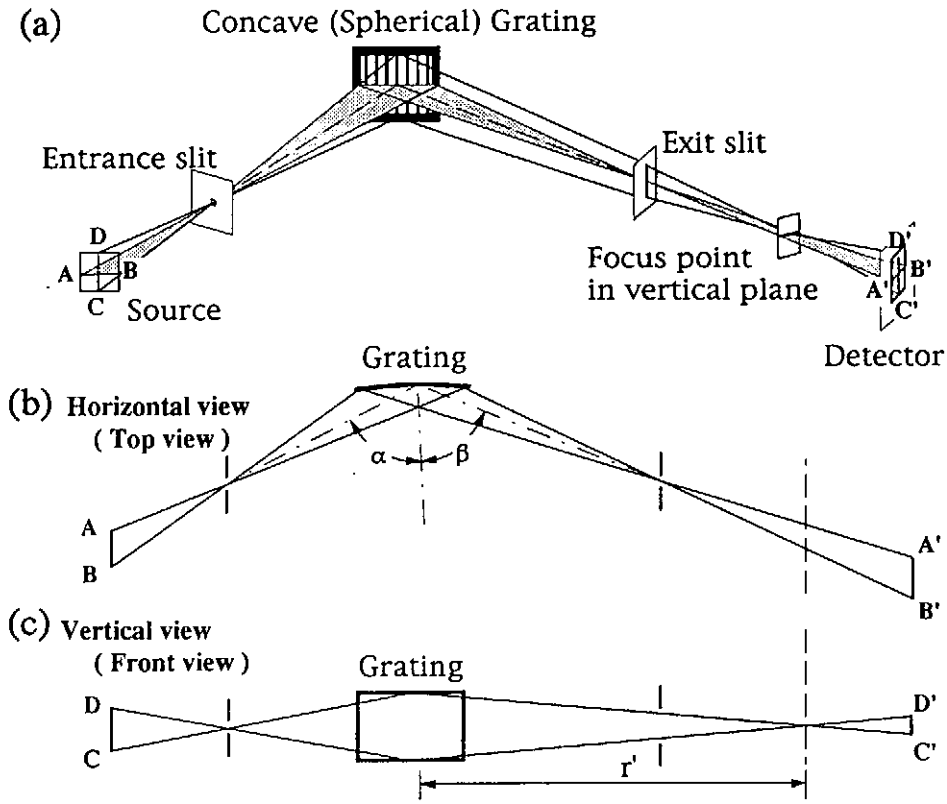

Fig. 2-1. (a) A schematic diagram of the optical system which has a spherical concave grating, an entrance slit with limited height, an exit slit and a two dimensional detector system, (b) View in the horizontal plane (the dispersion plane), (c) View in the vertical plane (perpendicular to the dispersion plane). A, B, C and D : source points. A', B', C' and D' : image points on the detector. α and β : the incidence and diffraction angle of the grating.

position of a point on the detector and where it originated in the source is accomplished. The important features of this scheme are two-dimensional imaging which does not require a stigmatic property for focusing. As a result, the monochromated two-dimensional space-resolved image of a plasma is obtained.

2.2 Off-Rowland Monochromator

A commercial 1-m normal incidence monochromator working on off-Rowland circle mounting is used for the imaging system.

The principle of off-Rowland monochromator action is that the grating is constrained to move along the bisector of the angle subtended by the slits at the center of the grating ; simultaneously the grating is rotated about a vertical axis tangent to its center (see Fig. 2-2). The rotation and the linear motion of the grating are provided with a lever arm attached to the grating mount. The end of the lever arm is constrained to a properly shaped cam for the best focusing (McPherson type normal incidence).

In this monochromator, the translation of the grating causes the shift of the optical axis from the center of the grating to the slits. The translation x (see Fig. 2-2) is given by

$$x \approx R \left[1 - \cos\{(\alpha + \beta)/2\} \right] \qquad (2-4)$$

where R is the radius of curvature of the grating, α and β are the angles of incidence and diffraction, respectively. The displacement of the

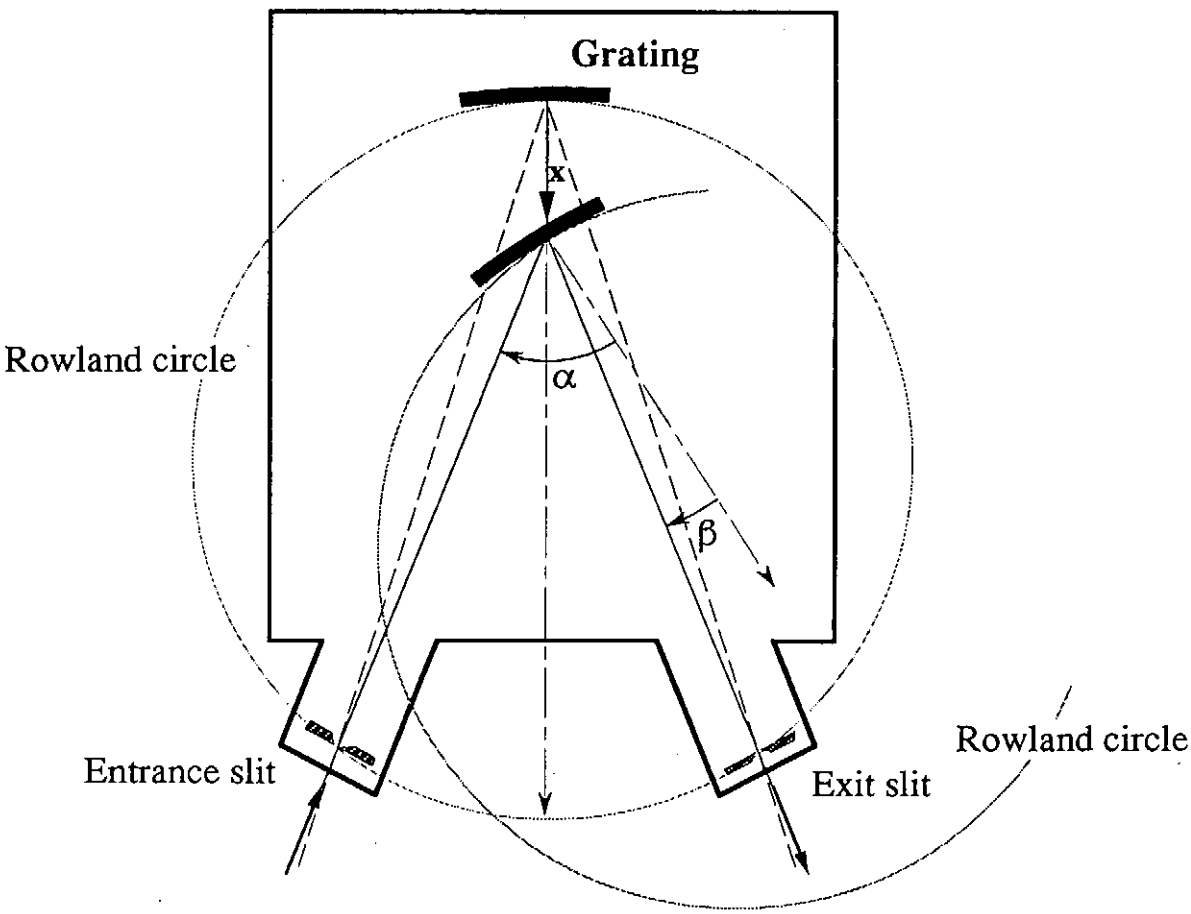

Fig. 2-2 Schematic of off-Rowland circle mounting monochromator based on the rotation and translation of the grating along the bisector of the angle subtended by the slits at the grating center.

optical axis is sufficiently small (0.2 mrad at 400 Å, 1.8 mrad at 1000 Å and 4 mrad at 1500 Å) for the use of observations of fusion oriented plasmas.

A commercial 1-m normal incidence monochromator with off-Rowland circle mounting fabricated by Acton research Co.(VM-521) is shown in Fig. 2-3. The angle subtended by the slits at the center of the grating is 15° in initial Rowland circle position.

The grating of ruled area 56 mm high (in the groove direction) and 96 mm wide is used to observe a large area of the plasma. The 1200-lines/mm grating blazed at 1500 Å is coated with Al + MgF_2. The grating efficiency as a function of wavelength is shown in Fig. 2-4, which is measured at 1st order.

Fig. 2-5 shows the measured profile for the spectral resolution, which is measured at the wavelength of Hg I 2536 Å. Measured spectral resolution is about 0.15 Å through the VUV wavelength region.

The spatial coverage are 5.5° in the dispersion plane (horizontal plane) and 3.2° in the direction perpendicular to the plane of dispersion (vertical plane). Two ports for the exit slits equipped in this monochromator can be alternated by using a rotatable reflection mirror positioned at the direction of the diffracted ray by the grating.

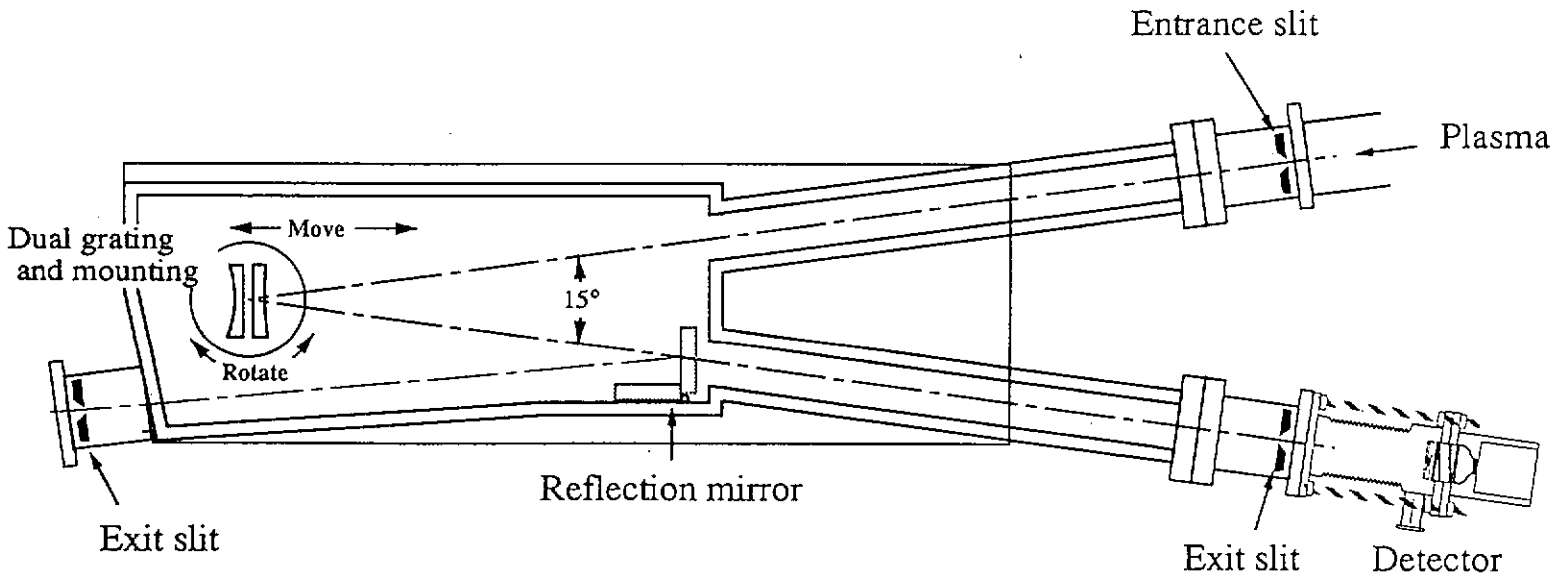

Fig. 2-3 A 1-m normal incidence monochromator with off-Rowland circle mounting which has a dual interchangeable grating mount. Detector system is shown outside of the exit slit.

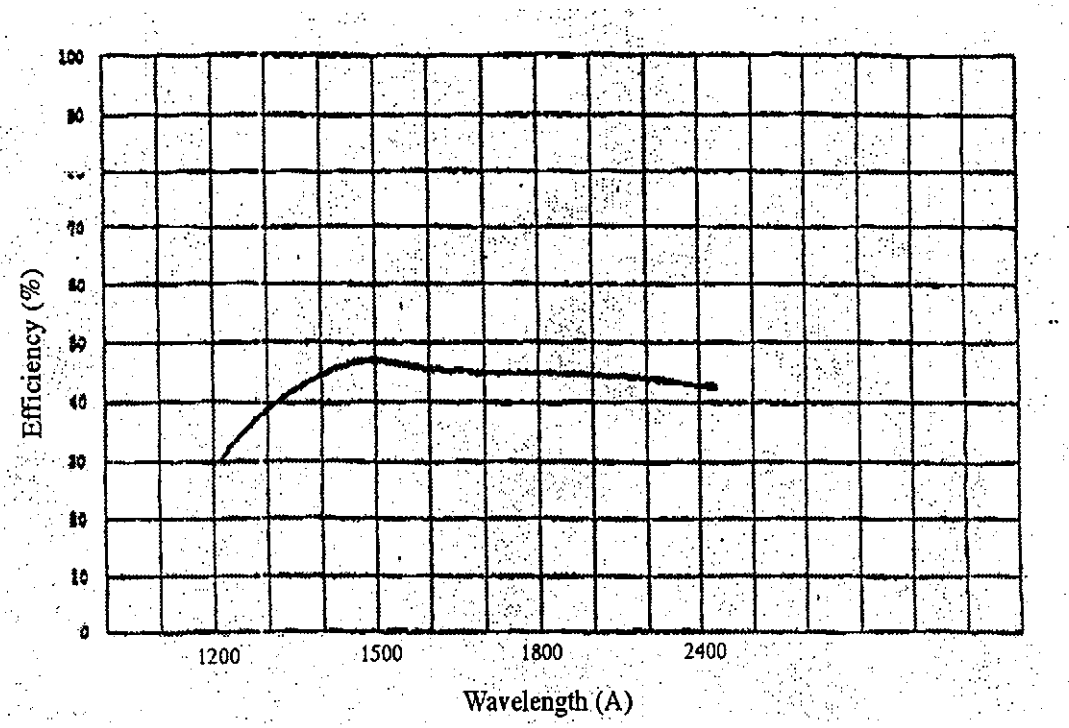

Fig. 2-4 Grating efficiency as a function of wavelength.
The grating is coated with Al + MgF_2 and blazed at 1500 Å.

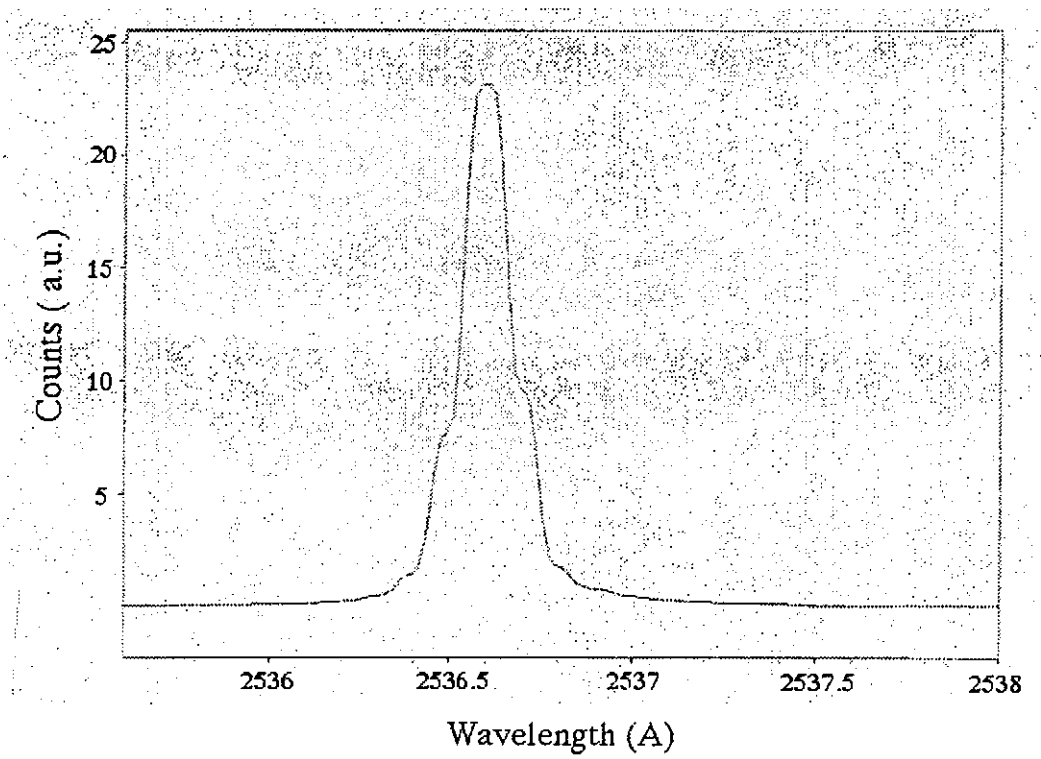

Fig. 2-5 Measured Profile for spectral resolution of the 1-m normal incidence monochromator with the 1200-lines/mm grating and the entrance slit width of 20 μm, which is measured at the wavelength of Hg I 2536 Å.

2.3 Detector System

The 2-D detector system for the spatial resolved images is shown in Fig. 2-6, which has a flexible bellows with guide bars.

The detector system consists of two subsystems: a microchannel plate (MCP) image intensifier assembly and a charge coupled device (CCD) camera, which is displaced away from the exit slit in order to obtain two-dimensional monochromatic images.

The MCP assembly consists of two 32 mmϕ microchannel plates in a chevron configuration and a P-20 phosphor screen which converts an electron into a visible photon (F2224-21PFFX, Hamamatsu photonics Inc.). The MCP used here has 12-μm-diam channels, with a 15-μm center-to-center spacing. The front surface of the MCP is coated with a 2500-Å thickness of CsI in order to enhance the quantum efficiency in the VUV wavelength region. Efficiency of the detector coated with CsI is given in Fig. 2-7 as a function of wavelength.

The bias angle of each microchannel used here is 8°. Relative sensitivity versus the incidence angle to the MCP is given in Fig. 2-8. When the focused lights by the spherical concave grating are diverged again and then illuminated on the detector(see Fig. 2-1), the incidence angle for each pixel of the MCP are changed around 8° ± 2°, which can influence on the spatial sensitivity of the detected image within the 10% errors.

The MCP operating voltage is varied from -1200 to -1800V depending on applications. The gain of the MCP versus the supplied voltage is shown in Fig. 2-9. Over this range the electron gain of the 2-stage MCP varies from 4×10^5 to 5×10^6.

Focusing of electrons is achieved by applying a voltage of +3 kV between the grounded MCP output surface and phosphor screen. The phosphor layer provides a gain of the order of 10-100 visible photons/incident 3-keV electron[10].

Fiber-optic 3:1 reducing taper couples the image of the phosphor to the CCD camera with fiber windows (C4346, Hamamatsu photonics Inc.).

The CCD camera of 768×493 pixels is used. The pitch of each pixel is 16.6 μm and 20 μm in horizontal and vertical direction, respectively, and the whole area of the device is 12.8×9.6 mm^2. The resolution of an image taken by this CCD camera is 8 bit. The 1-frame signal integrated during 33 msec from the camera is digitized by a video frame grabber (IQ-50, Hamamatsu photonics Inc.) and is analyzed by using a personal computer (Apple Macintosh).

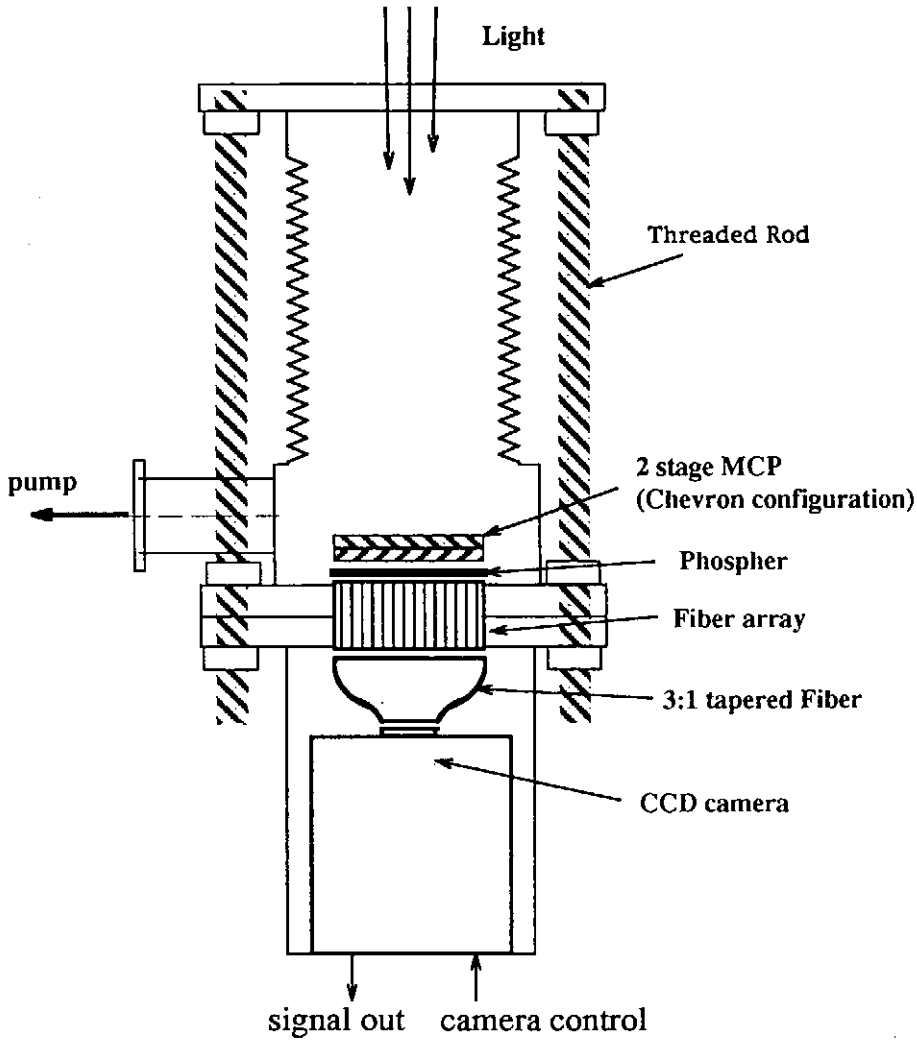

Fig. 2-6 Detector system which consists of a two-stage microchannel plate (MCP) image intensifier assembly and a charge coupled device (CCD) camera.

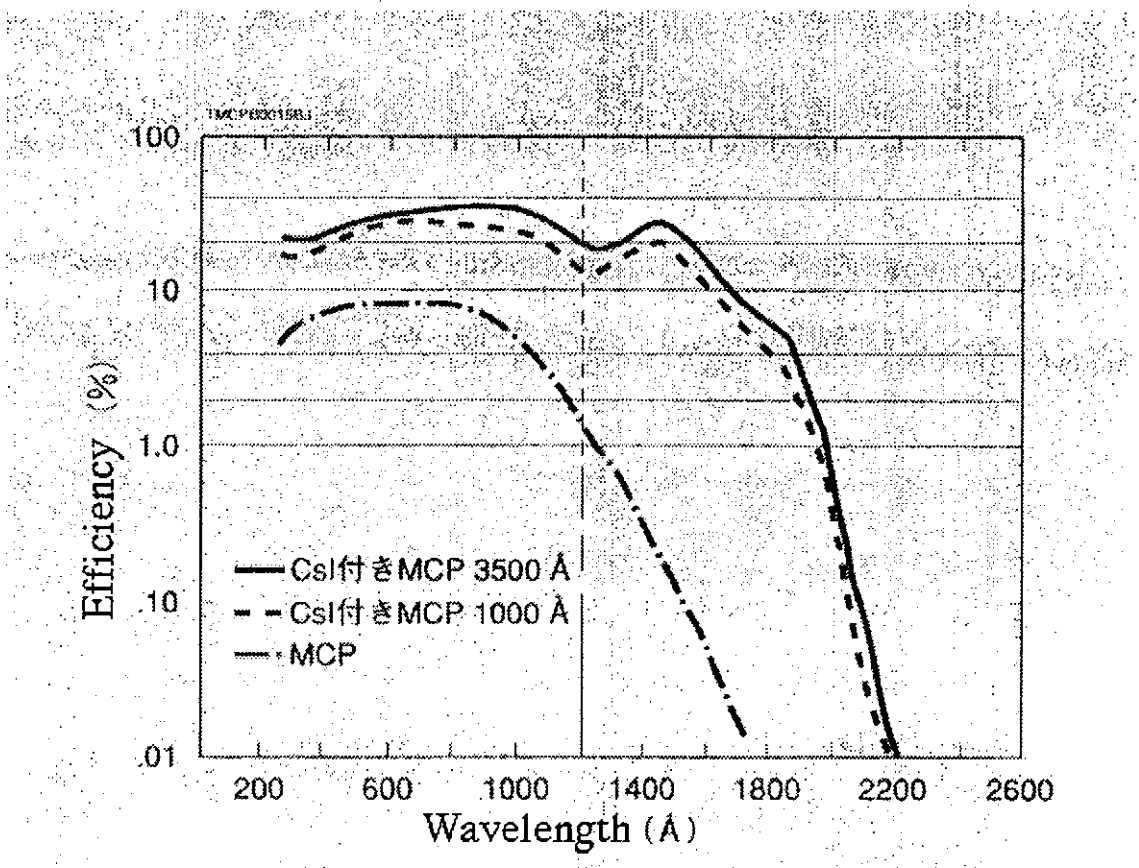

Fig. 2-7 Efficiency of the detector coated with CsI as a function of wavelength.

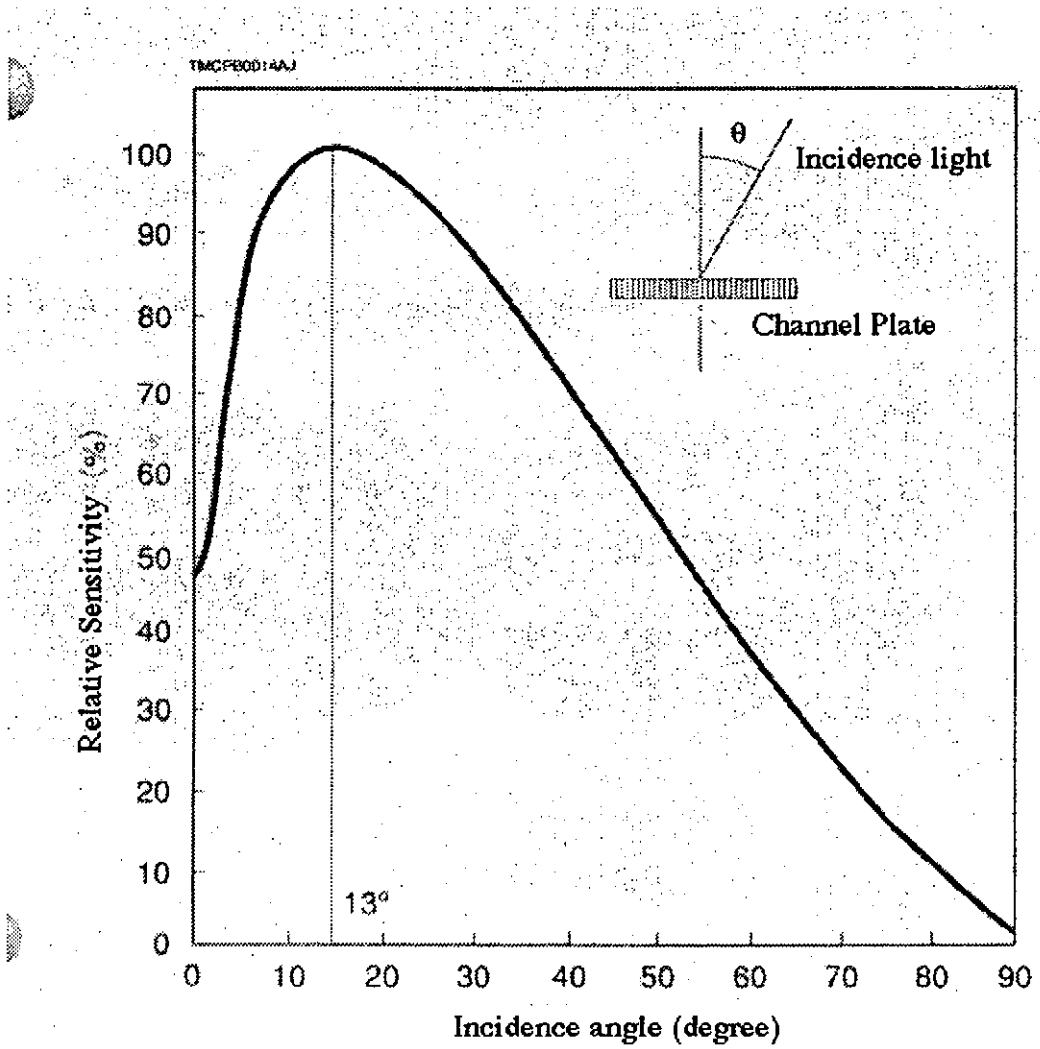

Fig. 2-8 Relative sensitivity as a function of the incidence angle to the MCP.

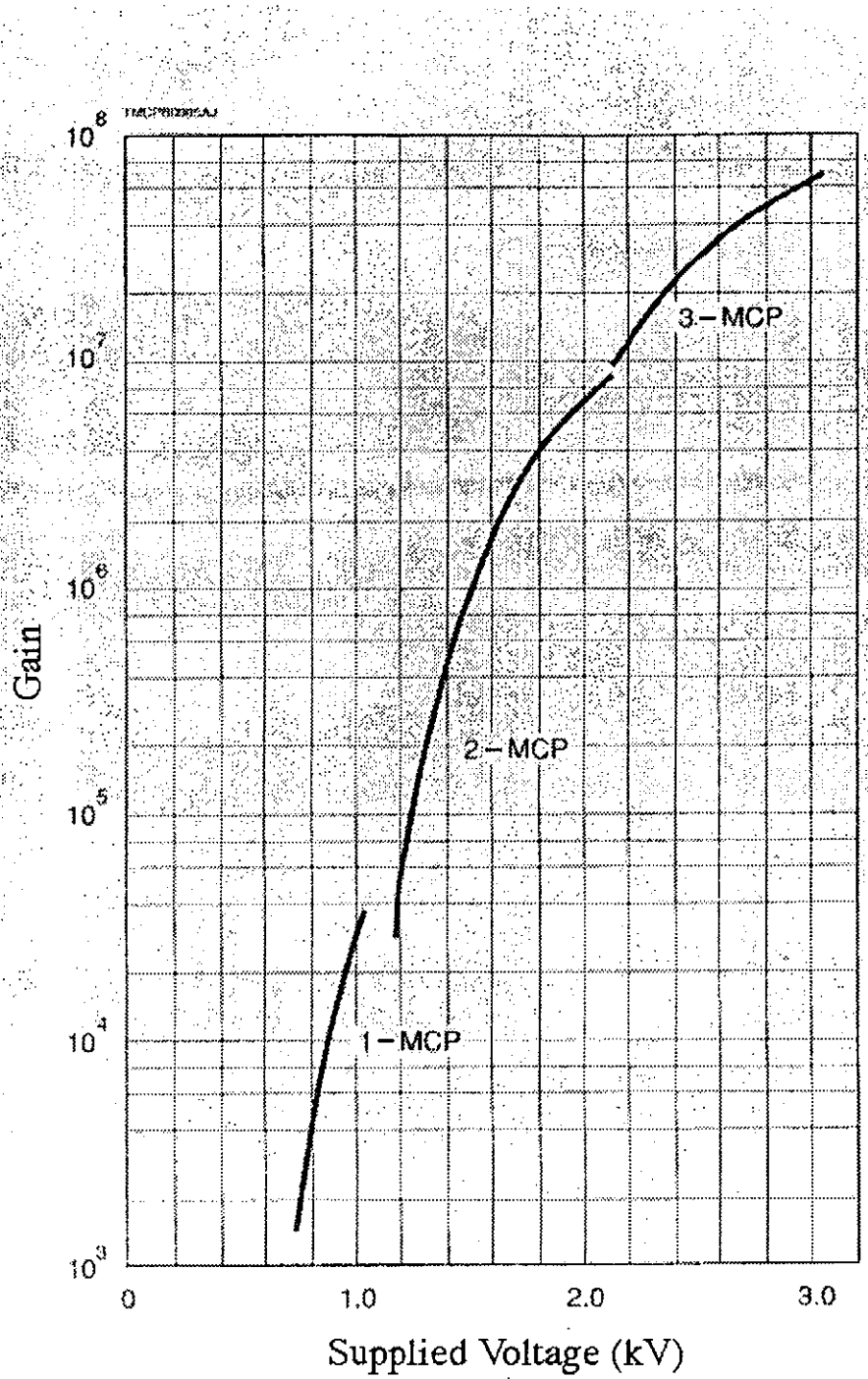

Fig. 2-9 The gain of the MCP versus supplied voltage.

3. Ray Tracing and Aberration

3.1 Aberration

The effect of astigmatism and coma are the major aberration inherited by the spherical concave grating. The theory of the astigmatism of a concave grating using the Rowland mounting was first developed by Runge and Mannkopf.[11] Later it has been dealt with in detail by Beuttler[12] and Namioka.[13, 14, 15, 16] In the following paragraphs, the study for astigmatism and coma is summarized briefly and applied to the imaging system using off-Rowland mounting.

The monochromatic image on the exit slit for a point source on the entrance slit is not a point but a line because of astigmatism; that is, focusing is achieved only in the horizontal plane.

In general, the astigmatic image is not a straight line. The curvature of the images identified two types of curvature. The curved spectral lines caused by the astigmatism of a point source at the entrance slit was called the *astigmatic curvature*. Another kind of curvature is caused by the finite length of the entrance slit, and was called by Beutler the *enveloping curvature*. The images at the exit slit have a curvature and height.

For the off-Rowland mounting, ray tracing has been performed to understand the aberration properties especially for astigmatism and coma.

Ray traced images on the exit slit are shown in Fig. 3-1 (a), (b), and (c), for the width of the entrance slit of 10 μm, 50 μm, and 100 μm, respectively. In this case, the entrance slit height is fixed to 0.1 mm and

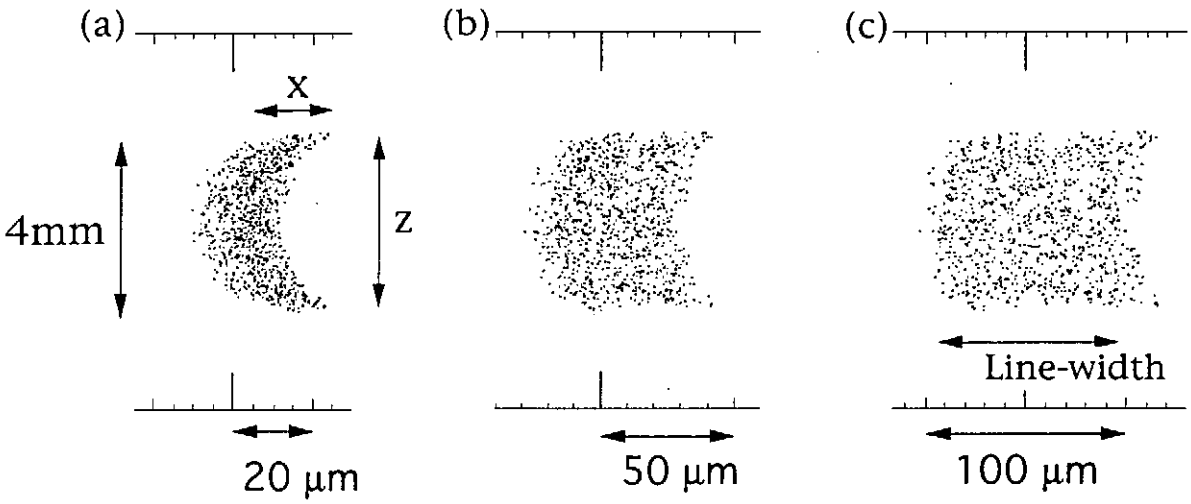

Fig. 3-1 Ray traced images at the exit slit plane for the off-Rowland mounting with the entrance slit width of 10 μm (a), 50 μm (b), and 100 μm (c) as a parameter. The entrance slit height of 0.1 mm and wavelength of 1500 Å are used.

the wavelength of the incidence photons is chosen to 1500 Å as a typical case.

The lengths of the astigmatic image z are 4 mm for the entrance slit of 0.1 mm height. In the case the width of the entrance slit is less than 50 μm, the line-width of the image on the exit slit is about 2 or 3 times greater than the width of the entrance slit. When the width of the entrance slit is larger than 50 μm, the line-widths of the images at the exit slit plane are almost same order of the width of the entrance slit.

3.2 Image Properties of the System

In order to study the spatial imaging properties of the off-Rowland mounting in the practical geometric configuration, we performed ray tracing calculations with the SHADOW computer program.[17, 18]

In this simulation, the sources are placed on a plane defined by axes x_s and z_s in Fig. 3-2, which is perpendicular to the optical axis. The intensity distribution of the source is assumed as uniform. The size of the source is limited by the acceptance angles of the monochromator. The source is set 30 cm away from the entrance slit. Rays starting from a point of the source plane go through the opening of the entrance slit and incident on the grating. The direction cosines of the diffracted rays are then calculated by using the light path function and Fermat's principle.[11] Then, the diffracted rays go through the exit slit. Finally the image point can be obtained on the output plane defined by axes x_i and z_i in Fig. 3-2, which is perpendicular to the optical axis.

Ray tracings using the off-Rowland mounting have been performed for a 1-m spherical concave grating which was 56 mm high (in the groove direction) and 96 mm wide, with a ruling of 1200 lines/mm, an entrance slit of 20 μm wide and 100 μm high.

In order to verify the reproduction of the object image, a source which has a cross shape has been used for ray tracing. Results of the ray tracings are shown in Fig. 3-2 where the wavelength of 1000 Å is assumed. Ray traced image at the output plane which is 30 cm away from the exit slit shows the good reproduction of the source (shown in Fig. 3-2(b)). These results of calculations show that the major aberrations (astigmatism, coma, astigmatic curvature) do not distort a imaging property seriously. We can make mapping the source position at the plasma on the detector plane from these results.

Another ray tracings have been performed to understand the characteristics of the images for the system. Ray traced spectral images with wavelength of 1500 Å is shown in Fig. 3-3 where the uniform source plane of 2.8 cm × 1.6 cm areas is assumed (shown in Fig. 3-3(a)). Fig. 3-3 (b) and (b') show the diffracted images on the exit slit, which represent aberration from the concave spherical grating. Fig. 3-3 (b') used different units against each axes. Focused image at the vertical focus position in the vertical plane is shown in Fig. 3-3 (c). The variation of the vertical focus position as a function of the wavelength is studied in section 3.3. The computed images at the output plane which is 30 cm away from the exit slit show the good reproduction of the plane source (shown in Fig. 3-3(d)).

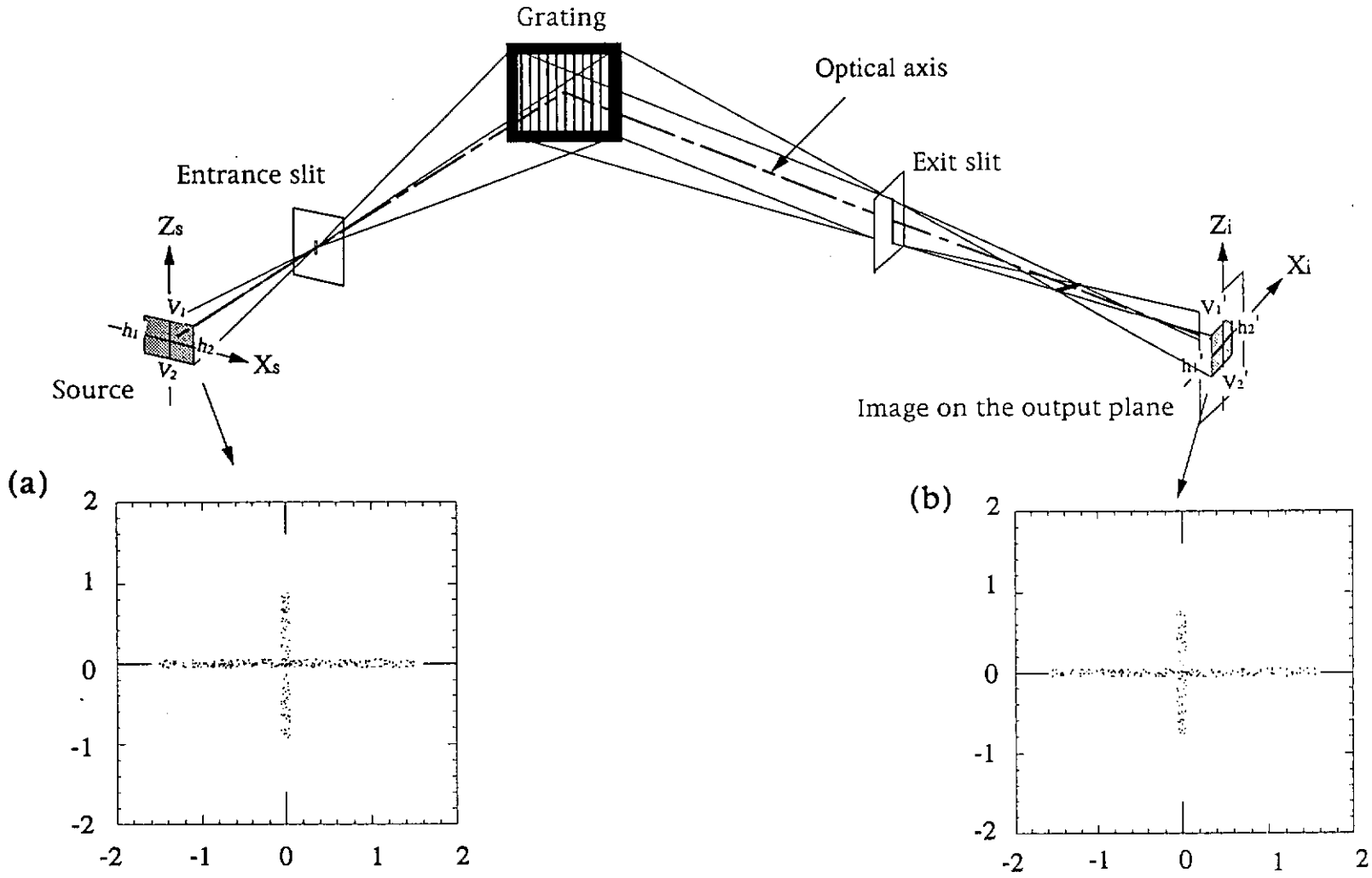

Fig. 3-2 Results of the ray tracings where the wavelength of 1000 Å is assumed.

(a) Cross type source. (b) Ray traced image on the output plane which is positioned 30 cm away from the exit slit.

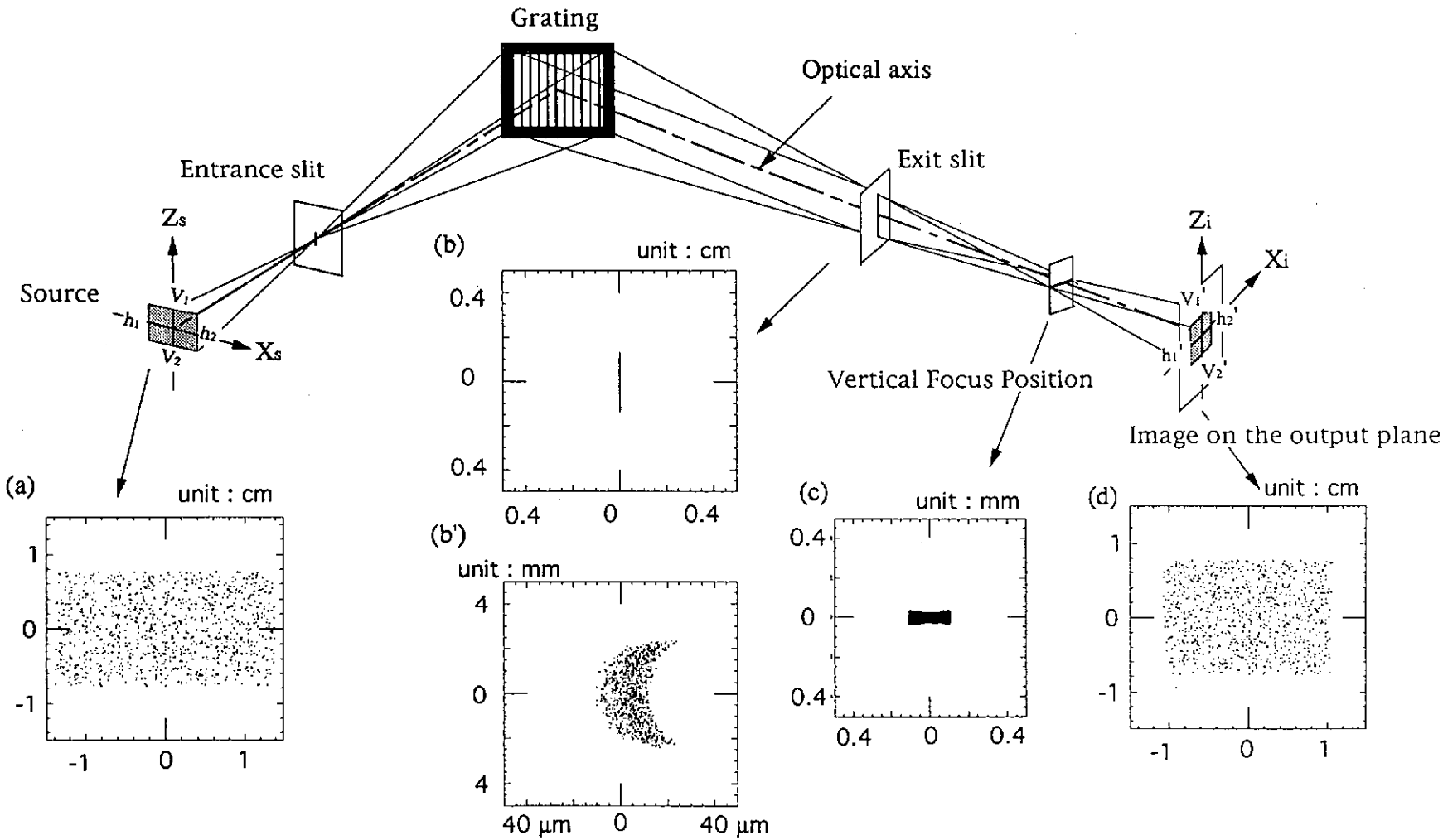

Fig. 3-3. Ray traced spectral images with wavelength of 1500 Å and an entrance slit of 0.02mm width and 0.1 mm height. (a) Plane source. (b) Image at the exit slit plane. (c) Image at the vertical focal plane. (d) Image at the output plane

3.3 Focusing Property of the Imaging System

In near normal incidence, the focusing position of the grating in the vertical plane is in outside across the exit slit, which is a function of the wavelength. Therefore, the monochromated imaging is achieved by displacing a two-dimensional detector away from the exit slit. In order to get the most suitable parameters between the exit slit and the detector system, the ray tracing was carried out to find the focusing position in the vertical plane as a function of the wavelength.

Ray tracing has been performed for a 1-m off-Rowland monochromator of an entrance slit 100-μm wide and 0.1-mm high, and wavelengths in the region from 1 Å to 3000 Å.

Results of ray tracings are shown in Fig. 3-4 where the focus distance in the vertical plane are measured from the exit slit along the optical axis (shown in Fig. 3-1). It shows that the vertical focus positions move to far away from the exit slit as the wavelengths increase. In the range of VUV wavelengths, the vertical focus distance is positioned between ~ 5 cm and 10 cm. As this results, 2-D detector for the imaging should be put more than 20 cm away from the exit slit depending on the size of 2-D detector.

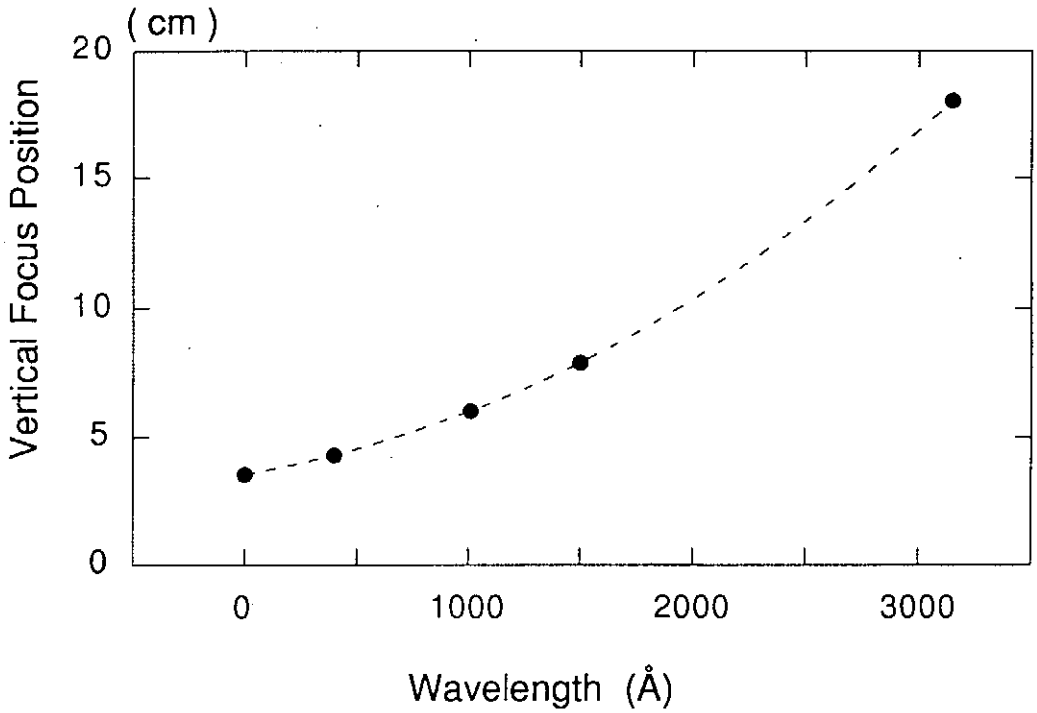

Fig. 3-4 The focus point from the exit slit in the vertical plane as a function of wavelength. A 1-m off-Rowland monochromator which has an entrance slit 100-μm wide and 0.1-mm high is used for ray tracing.

4. Arc discharge Light Source

4.1 Stationary Arc Discharge Light Source (TPD-S)

In order to see the spatial resolution and the relative sensitivity on spatial coverage of the imaging system in vacuum ultraviolet wavelength region, a stationary arc discharge has been developed as a light source.

Fig. 4-1 shows the configuration of the stationary arc discharge source (TPD-S: Test Plasma by Direct current discharge for Spectroscopy). LaB_6 disk of 70 mm diameter supported with Ta was used as a material of the cathode, which can be moveable for the variance of the distance from the anode. The convergent float electrodes are made of SUS. The anode made of Ta has a tiny nozzle of 8 mm diameter. The anode and float electrodes are water cooled not to be damaged by plasma heat.

A continuously operated dc arc discharges with the help of a sufficient magnetic field produce a steady state plasma at subatmospheric pressures. The plasma expands through the nozzle of the floating electrode and the anode into a low-pressure vessel, creating a supersonically expanding plasma jet.

The argon plasma is produced with the discharge current of 100 A, the discharge voltage of 100 V and the magnetic flux density of several hundred G. Electron temperature T_e and electron density n_e of the plasma are expected to be about 5 eV and 10^{14} cm^{-3}, respectively. And the size of the produced plasma column has a length of 50 cm and a diameter increasing from 8 mm to a few centimeter.

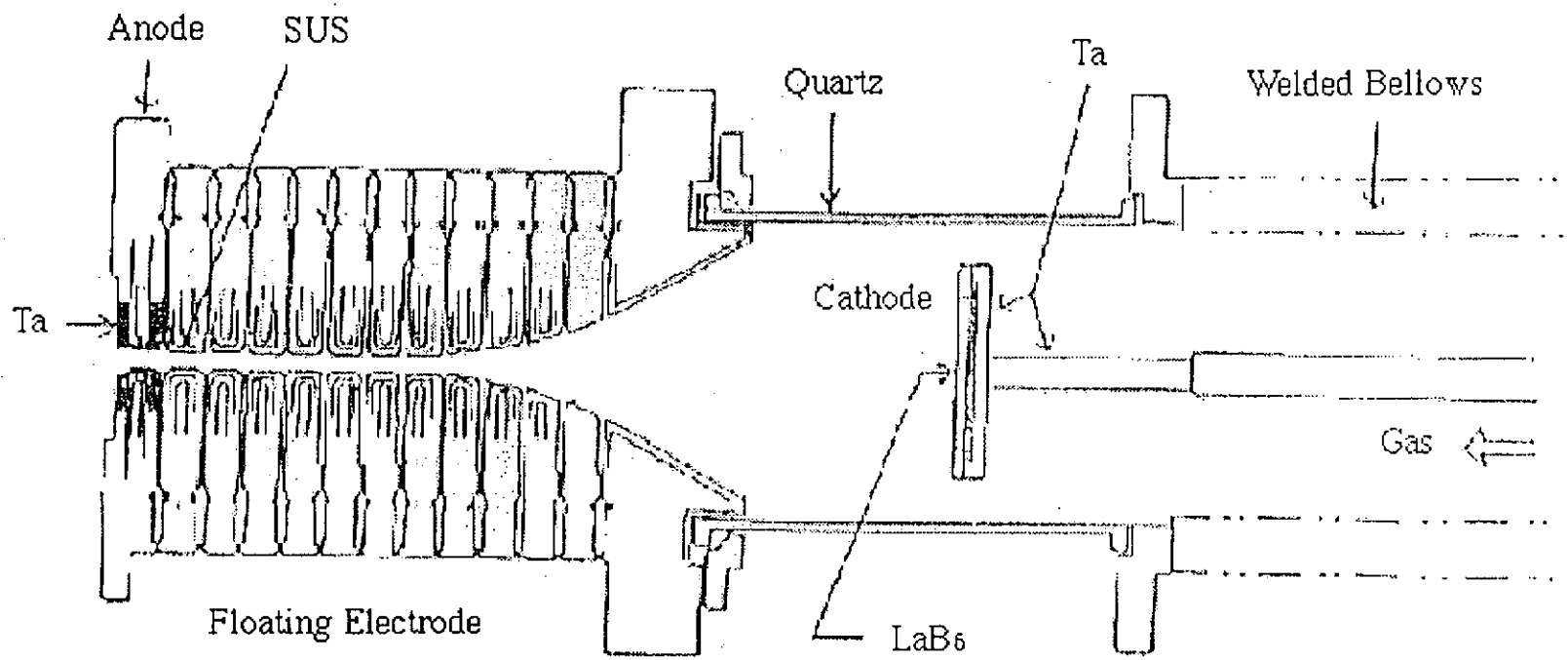

Fig. 4-1 Configuration of the TPD-S. A thermal plasma at subatmospheric pressure is created in a continuously operated dc arc, consisting of a cathode, floating electrodes and an anode plate. The plasma expands through the nozzle of the floating electrodes and anode into a low-pressure vessel, creating a supersonically expanding plasma jet.

4.2 Installation of the Imaging System to the TPD-S

The monochromator has been set to observe a part of the plasma column of the TPD-S in the direction perpendicular to the plasma axis (shown in Fig. 4-2).

The center of the viewing area of the monochromator was installed to see the plasma column at 30 cm behind from the anode. The viewing area is limited to 6 cm and 4 cm in the horizontal and vertical direction, respectively, because of the distance of 70 cm between the axis of the plasma column and the entrance slit of the monochromator.

Two gratings with 1200-lines/mm grooves can be interchangeable; one is a grating blazed at 1500 Å and another is a tripartite grating blazed at 800 Å.

2-stage MCP and CCD camera were installed to the distance of 30 cm behind from the exit slit. The signal from the CCD camera is analyzed by the Apple Macintosh (PowerPc 7100/75).

Monochromatic images of the plasma column were observed with spectral lines of Ar I at 1048 Å and Ar II at 932 Å, 718 Å.

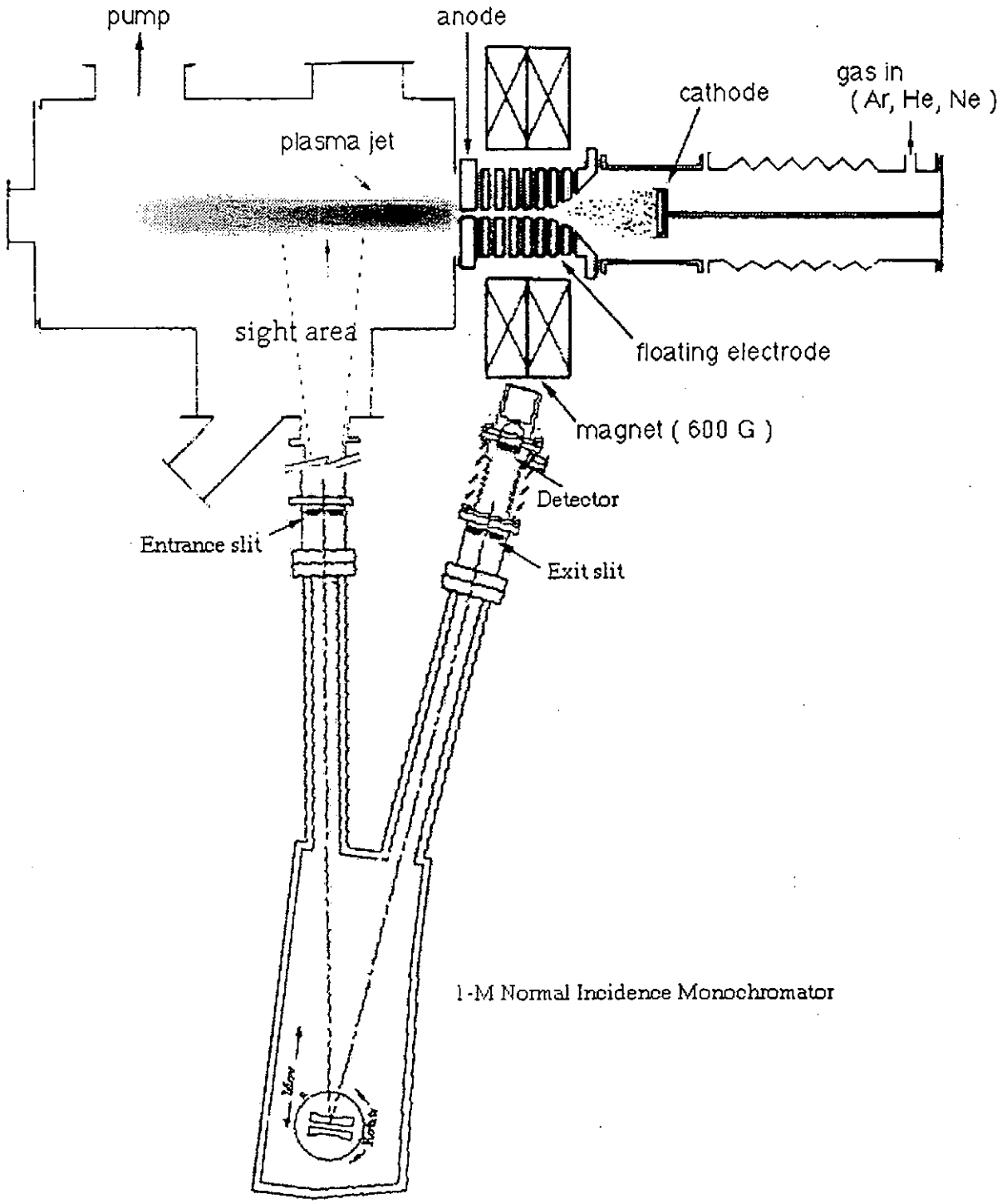

Fig. 4-2 Schematic diagram of TPD-S with the imaging system. The viewing area is limited to 6 cm and 4 cm in horizontal and vertical direction, respectively, and aligned to see the plasma column of 30 cm behind from the output of anode. Argon is used as the working gas.

5. System Performance

5.1 Vertical Focusing Test

To verify the results of ray tracing for the focusing property in the vertical direction, we used the experimental setup shown in Fig. 5-1.

A mercury lamp is used as a light source. The monochromated image of a mercury lamp was exposed on a photographic film (Polaroid 667).

Fig. 5-1 (a) shows a schematic diagram for the experiment of the vertical focusing test. A mercury lamp with 5 cm length in the vertical plane was positioned at a distance of 142 cm in front of the entrance slit with limited height of 0.5 mm. The photographic film was displaced at a distance of 30 cm behind from the exit slit. The image length of the mercury lamp was measured at zeroth order light, Hg I at 2536.5 Å and Hg I at 3131.5 Å.

A mercury lamp photographed by camera is shown in Fig. 5-1 (b). Fig. 5-1 (c) shows an image of a mercury lamp at the wavelength of 2536.5 Å as a typical example, which is exposed on a photographic film. These pictures simply show the attainment of monochromated imaging in this system and the demagnification scale depending on the vertical focusing point and the position of the film. Calculated image from ray tracing is represented in Fig. 5-1 (d), which use a rectangular source of 5 cm height and 1 mm width at the wavelength of 2536.5 Å.

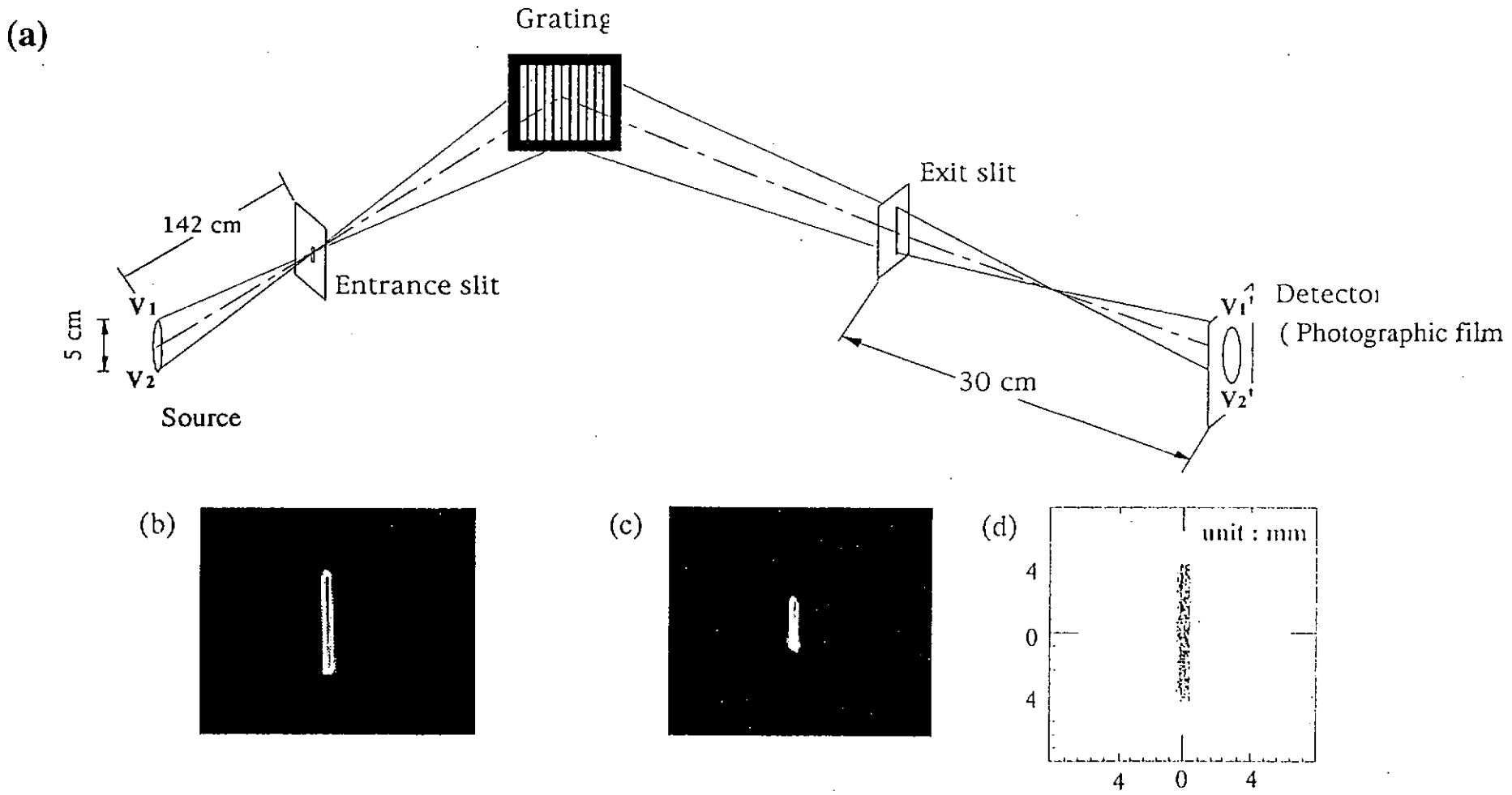

Fig. 5-1 The experimental setup using a Hg lamp for the focusing property in the vertical direction. (a) Schematic drawing for a vertical focusing test with Hg lamp. (b) Photograph of Hg lamp. (c) Image at Hg I 2536.5 Å exposed on the photographic film. (d) Ray traced image of 2536.5 Å.

The image length measured in the vertical direction was compared to the results of the ray-tracing calculations with the same experimental parameters (shown in Figure 5-2). In Fig. 5-2, the wavelength of 0 Å means the zeroth order light with the same entrance and diffraction angle of 7.5^0 in case of this monochromator. Measured image lengths are in good agreement with the results of ray-tracing.

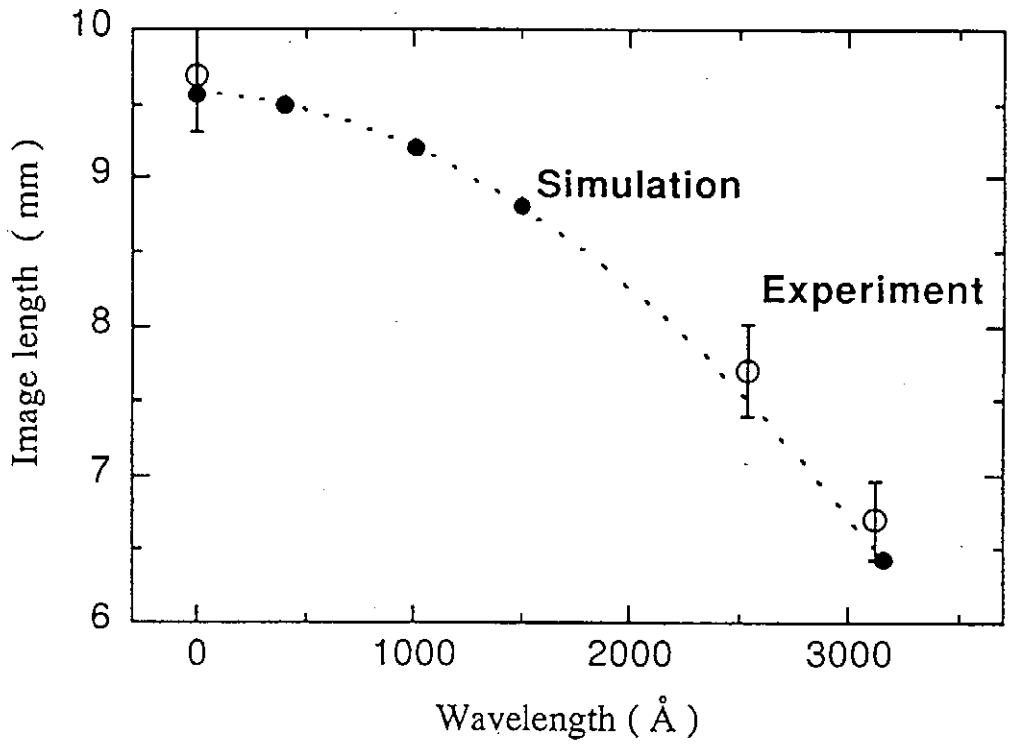

Fig. 5-2 Comparison of the observed image length with the ray-tracing calculation. The length of the mercury lamp was measured at zeroth order light, Hg I at 2536.5 Å and Hg I at 3131.5 Å

5.2 Spatial Resolution

In order to measure the spatial resolution of the imaging system, an aperture mask which has the apertures with various center pitches was inserted between the imaging system and the TPD-S device. The experimental setup is shown in Fig. 4-2. The 2-D detector system which is consist of MCP and CCD is set to the distance of 30 cm behind the exit slit.

An aperture mask has been settled to measure the spatial resolution of the 2-D imaging system (shown in Fig. 5-3 (a)). This mask is positioned at a distance of 40 cm in front of the entrance slit of the monochromator. The used masks have 1-mm, 1.5-mm or 2-mm diameter apertures opened with various center pitches.

The observed image of the aperture mask is shown in Fig. 5-3 (b). Images of the masks represent the spatial structure of light source in 2-dimensional plane. Here, the emission of Ar I 1048 Å from the plasma column was used as an illumination for the aperture mask.

The measured spatial resolution is about 0.5 mrad and 1 mrad in the dispersion and vertical plane, respectively, with an entrance slit of 0.1 mm width and height.

Better resolution can be obtained by decreasing the entrance slit width and height of the monochromator but at the expense of decreased signal to noise

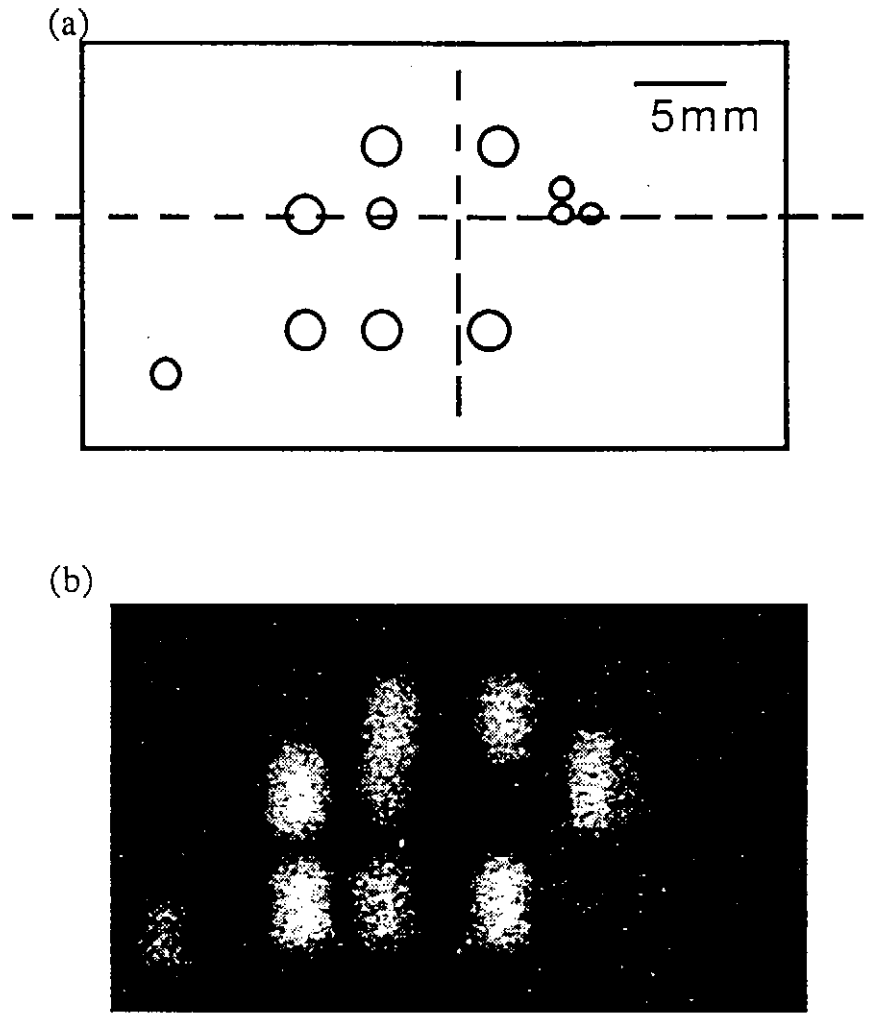

Fig. 5-3 Testing for spatial resolution. (a) An aperture mask with diameter of 2 mm, 1.5 mm and 1 mm holes. (b) The observed image of the aperture mask, where the entrance slit height of 1 mm and width of 0.5 mm were used.

5.3 Spatial Sensitivity

5.3.1 Preliminary Experiments using a Mercury Source

In order to understand the spatial sensitivity of the imaging system, a preliminary experiment using a mercury source has been performed.

The mercury lamp was just attached at the entrance slit with the 0.1 mm width and height to fill up the acceptance light cone of the grating, here Hg lamp acts as a homogeneous light source. The width of the exit slit was fixed to 0.1 mm. The photographic film (Polaroid 667) positioned at a distance of 30 cm behind the exit slit was used to expose the monochromated image of a homogeneous source. The grating which has the blaze wavelength at 1500 Å was used. Images of a mercury lamp have been measured at zeroth order light (CI : the central image), Hg I at 2536.5 Å and 3131.5 Å.

Fig. 5-4 shows the image at Hg I 2536.5 Å on the photographic film and its intensity profile. The good uniformity of the spatial sensitivity was concluded perpendicular to the dispersion direction. However, it was found that there is a strong non-uniformity of the sensitivity in the direction of the dispersion plane.

An image measured at zeroth order light is shown in Fig. 5-5, as an other example. The direction of the non-uniformity of the spatial sensitivity in the direction of the dispersion plane was reversed compared to the image at Hg I 2536.5 Å, though the uniformity in the vertical direction is confirmed.

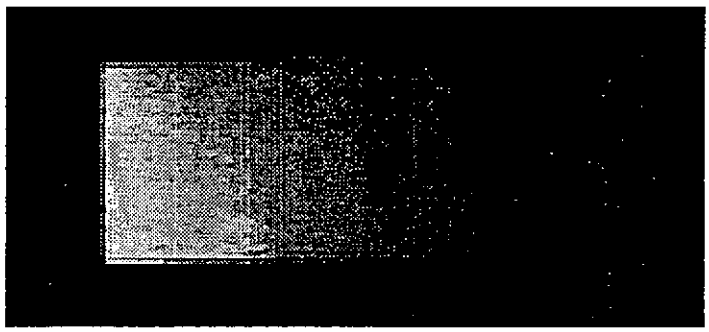

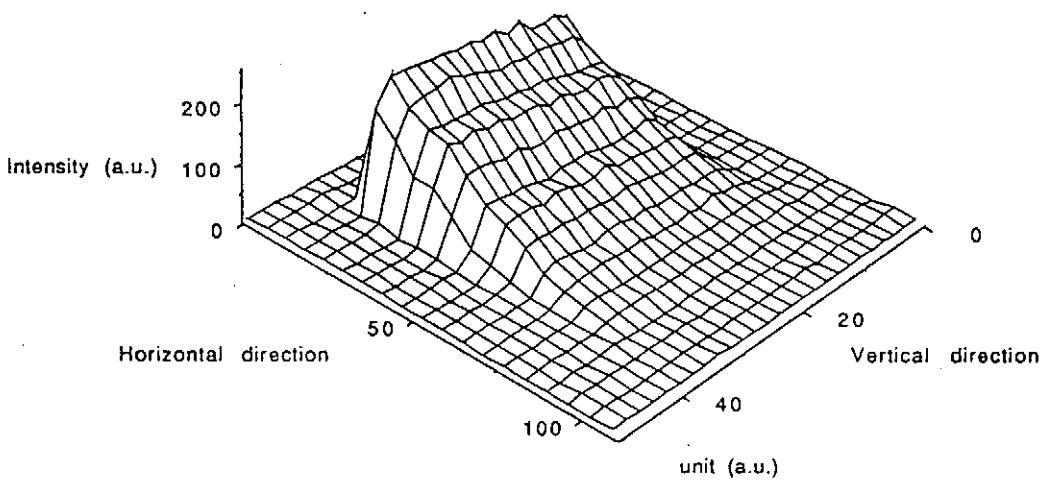

Fig. 5-4 Image and its profile at Hg I 2536.5 Å.

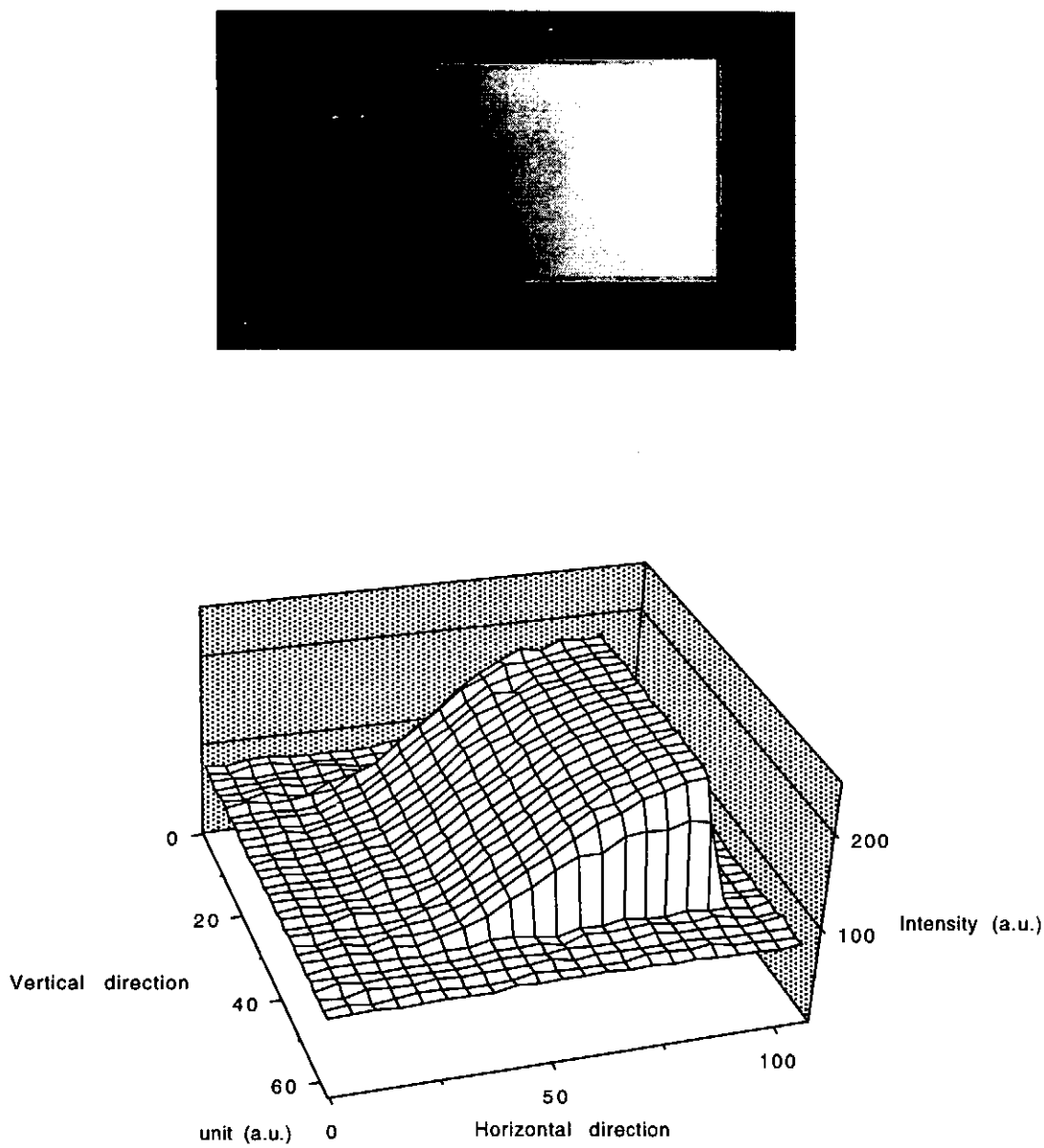

Fig. 5-5 Image and its profile measured at zeroth order light.

5.3.2 Effects of a Grating on the Horizontal Sensitivity

The strong variation in the horizontal sensitivity is explained as the effect of a grating.

a) A grating

Gratings are usually blazed, which means that the groove is shaped to concentrate a large fraction of the incident intensity into diffraction at a particular angle. The principle of the concentration of radiation into any desired spectrum is discussed below.

A cross section of a typical blazed grating is shown in Fig. 5-6. Let N be the normal to the macroscopic surface of the grating while N' denotes the normal to the facets. The grooves are cut such that the facets make an angle θ with the grating surface. The angles α and β are the angles of incidence and diffraction. The principle of concentrating entrance radiation into a given wavelength is that this wavelength must be diffracted in a direction which coincides with the direction of the specularly reflected light from the surface of the facet.

The wavelength λ_{blaze} for which the grating is blazed is given by

$$m\,\lambda_{blaze} = 2d \sin\theta \cos(\alpha - \theta) \qquad (5-1)$$

For the $\alpha = 0$ and m=1, λ_{blaze} is normally defined as the blaze wavelength, and it is obviously fixed by the grating ruling. The grating is also blazed for the higher order of $\lambda_{blaze}/2$, $\lambda_{blaze}/3$ and etc.

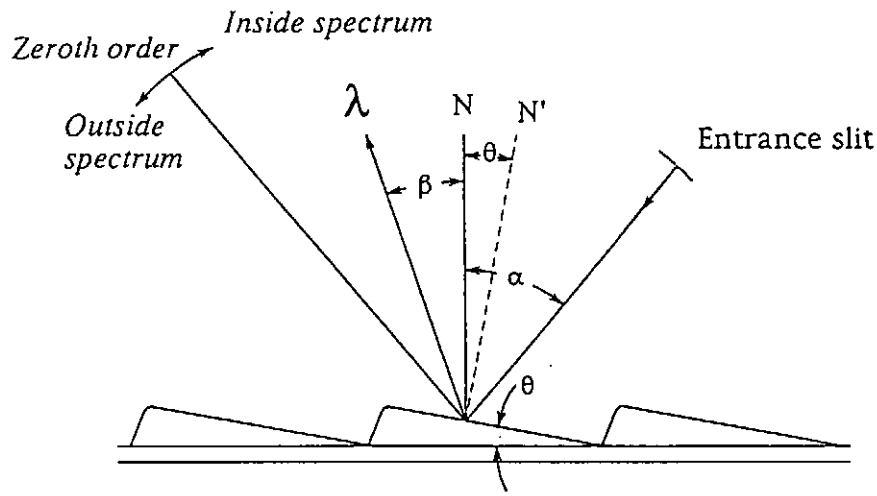

Fig. 5-6 A cross section of a typical blazed grating. N and N' are the normals to the grating and the facets respectively. θ is the angle between the facets and the grating surface. The angles α and β are the angles of incidence and diffraction.

b) Effect of the blazed facet plane

Effect of the blazed concave grating on the intensity distribution is discussed.

The width of one facet of a grating is the same order of length as the wavelength of the entrance ray. In our case with 1200 grooves/mm grating, the width of one facet is about 8000 Å, for example. For a rigorous treatment of intensity distributions from such a grating, electromagnetic wave form given by Sommerfeld is calculated. But this rigorous treatment of diffraction problem provides a complicated mathematical formulation. Another approach based on the Fraunhofer diffraction is practically useful to see the intensity distribution from a grating. Qualitatively speaking, Fraunhofer diffraction occurs when both the incidence and diffracted waves are effectively plane. This will be the case when the distances from the source to the diffracting aperture and from the aperture to the receiving point are large enough for the curvatures of the incident and diffracted waves to be neglected.

In the case of Fraunhofer diffraction scheme, the Fresnel-Kirchhoff formula becomes to be a very simple equation

$$U = C \int \int e^{ikr} \, dA$$

where all constant factors have been lumped into one constant C. And U is a complex amplitude, k is a wave number and A is an aperture area. The formula above states that the distribution of the diffracted light is

obtained simply by integrating the phase factor e^{ikr} over the aperture.

The diffraction by a single slit is described in brief to see an intensity envelope and the case of the diffraction by the facet of the blazed grating is treated in the same way.

(1). The single slit

The case of diffraction by a single narrow slit can be treated as a one-dimensional problem. Let the slit be of length L and of width b. The element of area is then $dA = L\ dy$ as indicated in Fig. 5-7(a). Furthermore, we can express r as

$$r = r_o + y \sin\theta$$

where r_o is the value of r for $y = 0$, and where θ is the angle of diffraction.

The diffraction formula then yields

$$U = C e^{ikr_o} \int_{-b/2}^{b/2} e^{iky \sin\theta} L\, dy$$

$$= 2C e^{ikr_o} L \frac{\sin(\frac{1}{2} kb \sin\theta)}{k \sin\theta} = C' \left(\frac{\sin\beta}{\beta} \right)$$

where $\beta = (\pi b/\lambda) \times \sin\theta$, and $C' = e^{ikr_o} CLb$. Thus C' $(\sin\beta / \beta)$ is the total amplitude of the light diffracted in a given direction defined by β.

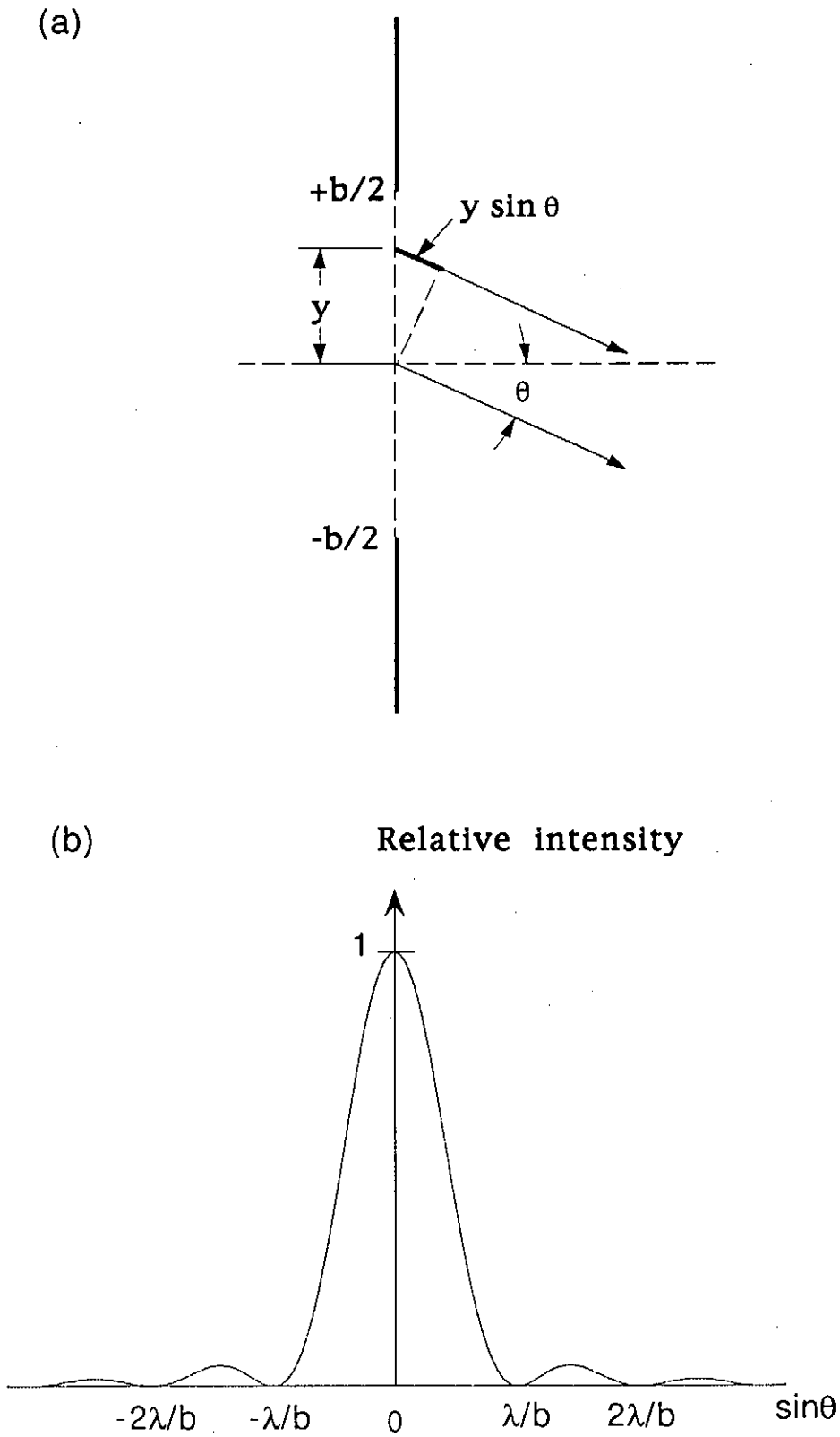

Fig. 5-7 Definition of the variables by a single slit and intensity distribution

And the corresponding intensity distribution at the infinity is given by the expression

$$I = |U|^2 = I_0 \left(\frac{\sin\beta}{\beta} \right)^2$$

where $I_o = |CLb|^2$, which is the intensity for $\theta = 0$. The intensity distribution is plotted in Fig. 5-7(b). The maximum value occurs at $\sin\theta = 0$, and zero values occur for $\sin\theta = \pm \lambda/b, \pm 2\lambda/b, \ldots$, and so forth.

(2). The facet plane of a grating

The case of diffraction by one facet plane is treated in the same way as the single slit (shown in Fig. 5-8). Let the facet be of groove length L and of width b. In here, the path difference $\Delta\phi$ of the two rays shown is expressed as

$$\Delta\phi = -y \times \sin\alpha + y \times \sin(\alpha + \gamma) = [\sin(\alpha + \gamma) - \sin\alpha] \times y$$

where α is the incidence angle, and γ is the angle between the direction of the mirror reflection and that of the diffracted light (in other word, angle of the diffracted light measured from the direction of the mirror reflection).

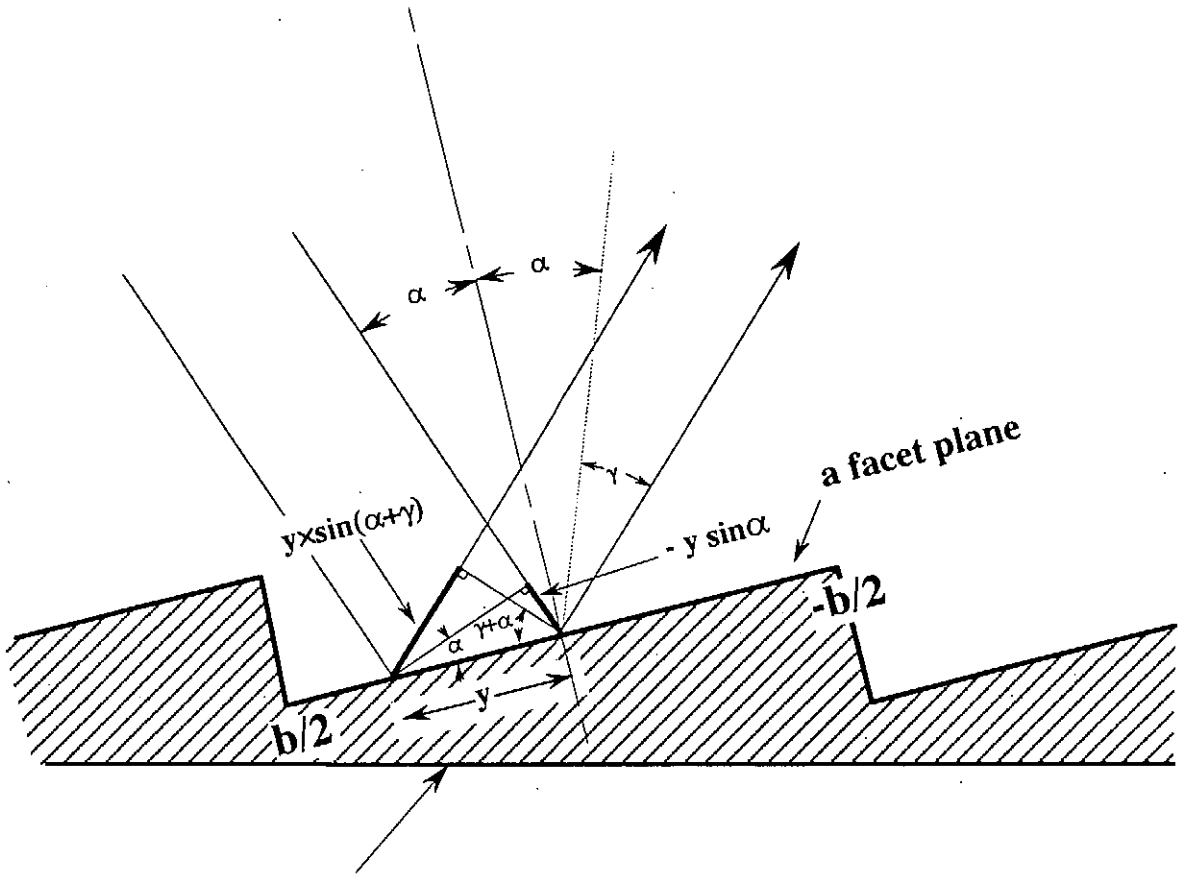

a cross section of the blazed grating

Fig. 5-8 Definition of the variables for Fraunhofer diffraction by a facet plane of the blazed grating

The result is

$$U = C e^{ikr_o} \int_{-b/2}^{b/2} e^{iky\,[\sin(\gamma+\alpha)-\sin\alpha]} L\, dy$$

$$= 2C\, e^{ikr_o} L \frac{\sin(\frac{1}{2} kb\,[\sin(\gamma+\alpha)-\sin\alpha])}{k\,[\sin(\gamma+\alpha)-\sin\alpha]} = C' \left(\frac{\sin\beta'}{\beta'}\right)$$

where β' and C' is $(\pi b/\lambda) \times [\sin(\alpha + \gamma) - \sin\alpha]$ and $e^{ikr_o} CLb$, respectively. Therefore, the corresponding intensity distribution at the infinity is given by

$$I = |U|^2 = I_0 \left(\frac{\sin\beta'}{\beta'}\right)^2$$

where $I_o = |CLb|^2$, which is the intensity for $\theta = 0$.

Diffracted patterns from one facet as a function of γ are shown in Fig. 5-9. It shows that the full width at half maximum (FWHM) becomes smaller at shorter wavelength.

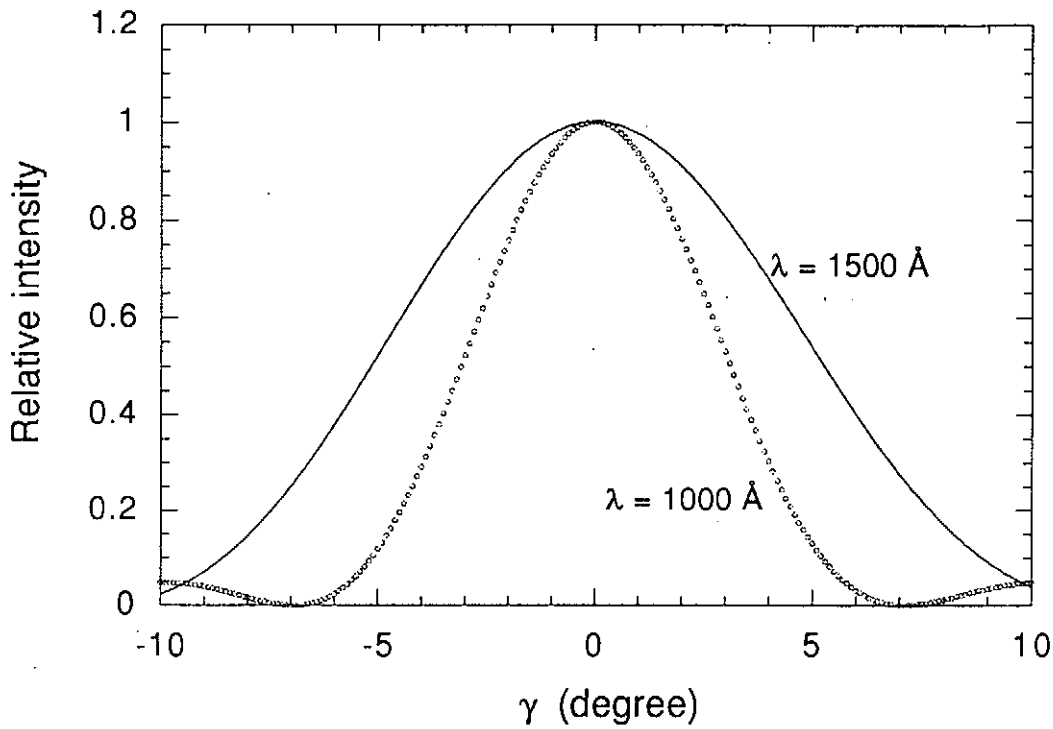

Fig. 5-9 Diffraction pattern of a facet as a function of γ.
γ : angle between the direction of the mirror reflection and that of diffracted light.
Here, the width of a facet b is set as 6400 Å corresponding to the grating with 1200 grooves/mm.

c) Intensity distribution by the blazed concave grating

Effect of the blazed concave grating on the horizontal sensitivity in the imaging system can be simply described by the difference between the exit angle of a diffracted light in consideration and the angle for the effective blazed wavelength.

The imaging system consists of the entrance slit, the spherical concave grating, the exit slit, and detector system.

The key point is that the detector should be positioned behind from the exit slit as shown in Figure 5-10 (a). When the detector is positioned on the exit slit, there is no spatial resolution in the dispersion plane since the diffracted monochromatic rays from the grating are focused to the exit slit forming a narrow line. When the detector is used at a distance behind the exit slit, however, intensity distribution on the detector is influenced by the effect of a diffraction from each facets.

As discussed in the preceding section, each facet plane makes an output of a diffraction pattern. The center (maximum intensity) of the diffraction pattern is in the direction of the mirror reflection against the facet plane (Define the angle β' as the direction of the mirror reflection to the grating normal). Fig. 5-10(b) shows the definition of the incidence and diffraction angles on a facet plane of the grating. But the direction of a measured wavelength makes an angle β that is measured from the normal to the grating plane, which is defined as the diffraction angle.

Therefore, the difference between the direction of the mirror

reflection and that of a measured wavelength has a responsibility for the intensity on the pixel of the detector. (Lets define the difference angle as γ ($= \beta - \beta'$))

For considering the intensity distribution on the detector, it is necessary to calculate the difference angles γ on all the facets of the grating.

Fig. 5-10 shows the schematic diagram of a typical blazed grating demonstrating the definitions (the incidence and diffraction angles to the grating normal and angles of the mirror reflection to the facet plane) against each area of the grating facet.

The grating of 96 mm width was used for the 1-m off-Rowland monochromator. The grating is blazed at 1500 Å, which means the blaze angle $\theta = 5.2°$.

In case of 1500 Å, the distance between the center of the grating and the entrance slit is varied to 98.7 cm, and the incidence angle of the grating is adjusted to 12.7 degree. Incidence angles on the facet of area 1, area 2 and area 3 are 12.9°, 12.7° and 12.5°, respectively.

At the center part of the grating (area 2), the diffracted light with the wavelength of 1500 Å has a diffraction angle of 2.3° to the grating normal, and here the diffraction angle for the effective blazed wavelength is also 2.3° to the grating normal. In the same way, the diffraction angle for 1500 Å at area 1 is 2.2° and that of the effective blazed wavelength is -3.4° to the grating normal. The diffraction angle for 1500 Å at area 3 is 2.4° and that of the effective blazed wavelength is 7.8°.

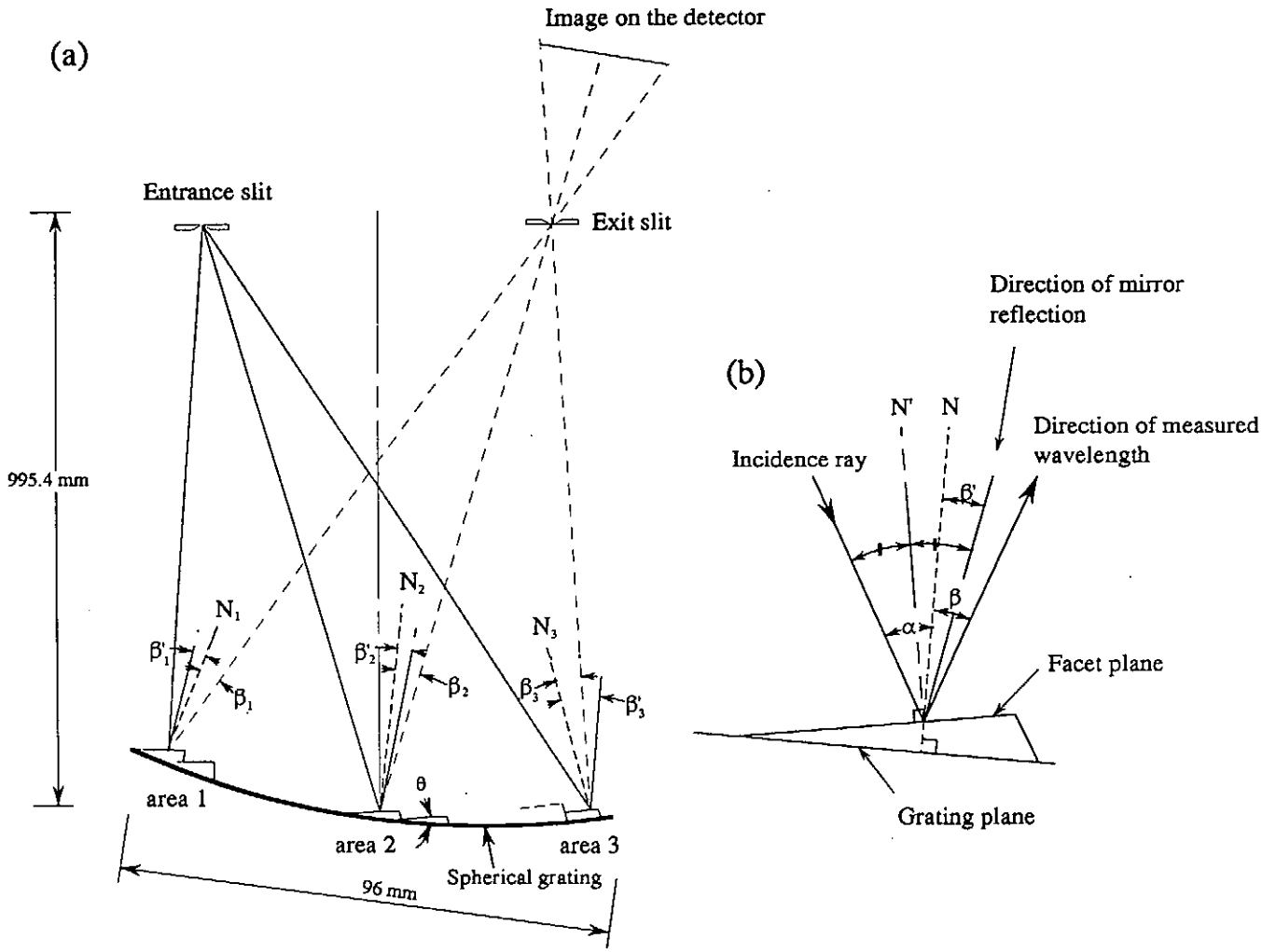

Fig. 5-10 Schematic of a typical blazed grating demonstrating the angles and its definition against three facets of the grating. The blazed angle θ of 5.2 degree is used, which is the angle between the facets and the grating surface. Radius of curvature of the spherical grating is 995.4 mm, and the grating of 96mm width is used. Here, β is the diffraction angle for the wavelength selected, and β ' is the diffraction angle for the effective blazed wavelength (angle for the mirror reflection from the facet plane). This figure is not to scale.

As the result, the angles (γ) between the direction of the mirror reflection and that of the diffraction for the selected wavelength are varied to -5°, 0°, and 5° from area 3 to area 1.

In the case of imaging of a wavelength far from the blazed wavelength, 1000 Å as an example, incidence angle α of 11.0° to the grating normal is selected. Then, the incidence angles at each facet are changed to 10.8°, 11° and 11.1° from area 3 to area 1. The difference between the diffraction angle and the angle for the effective blazed wavelength from a facet are varied to -2°, 3°, and 9° from area 3 toward area 1.

The difference between the diffraction angle and the angle for the effective blazed wavelength at a various wavelength are represented in Table 5.3.2.

Table 5.3.2 Difference angles γ for each area at various wavelengths.

(Unit : degree)

	Area 1	Area 2	Area 3
1548.2 Å	5.3	-0.2	-5.7
1238.8 Å	7.3	1.8	-3.7
1031.9 Å	8.7	3.0	-2.2
977 Å	9.1	3.5	-1.8
2536 Å	-2.1	-7.6	-13.1

These calculations show that when the grating is used to diffract the light which is of the wavelength close to the blazed wavelength, intensity distribution in the horizontal direction is appeared to have axis-symmetry and be roughly uniform.

On the contrary, in the case of an imaging measurement at a wavelength far from the blazed wavelength, the intensity distribution shows a strong non-uniformity, due to the large deviation between a diffraction angle and an angle for its effective blazed wavelength.

The above discussion may give us an explanation for the roughly uniform distribution or the strong variation in the horizontal sensitivity of the imaging system.

Observed intensity distributions of the C IV 1548.2 Å, N V 1238.8 Å and O VI 1031.9 Å (angle between the direction of the mirror reflection and that of diffracted light) are compared with calculated intensity envelopes as a function of γ, as given in Fig. 5-11.

Fairly good agreements between the observed intensity distribution and the expected distribution from the diffraction theory show that the non-uniformity of the imaging system in the horizontal direction is attributed to the effect of the concave grating.

To attain a more flat reflectivity over the entire surface of a grating, the grating which has different blaze angles in one surface is available commercially; the angle of the ruling diamond is reset in a few areas. Even though it increase the total intensity, this grating also does not produce a uniformity of the sensitivity in the dispersion direction.

Image from a tripartite grating is shown in Fig. 5-12 as an example. It is clearly seen that the spatial sensitivity of the tripartite grating represents three patterns in the dispersion direction.

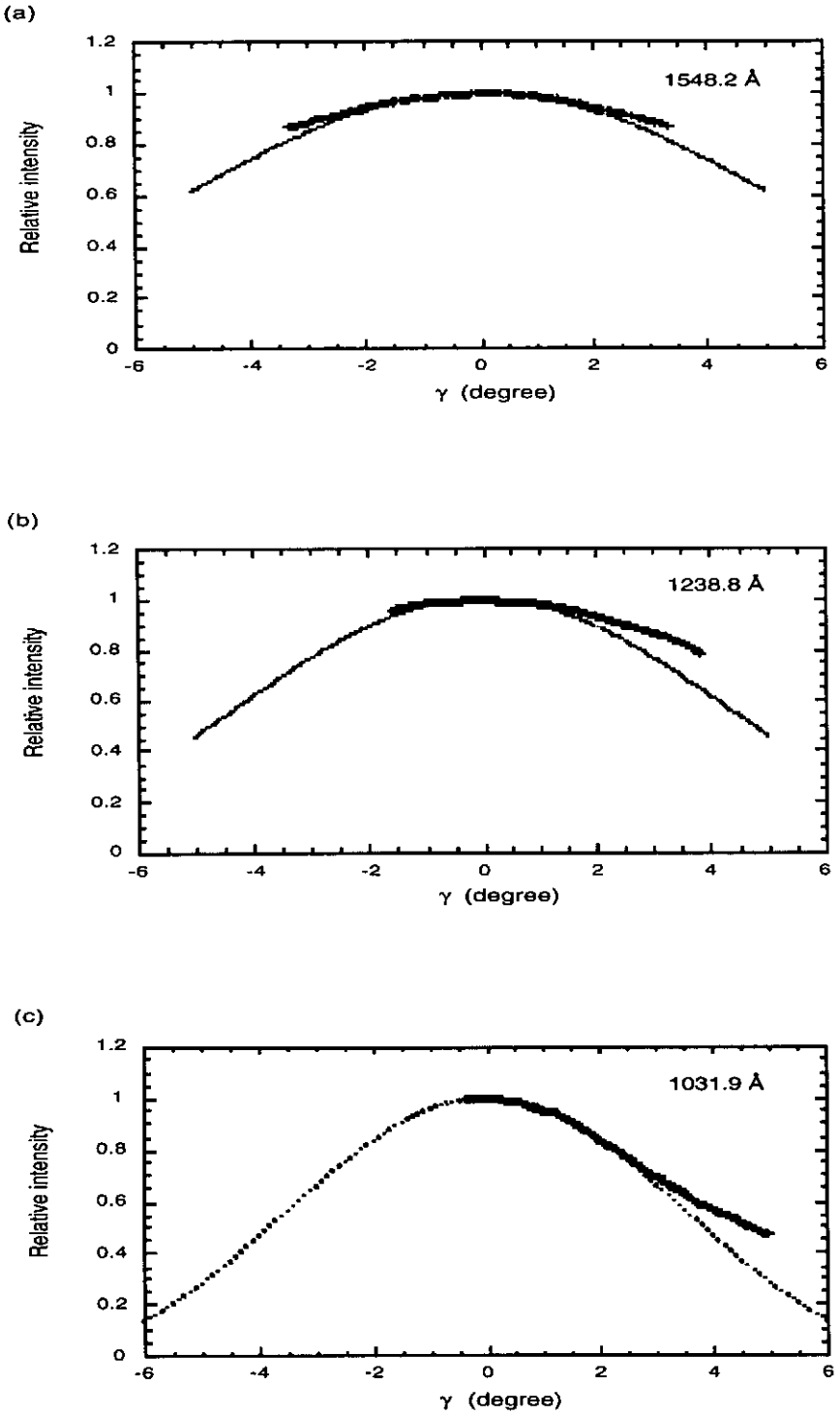

Fig. 5-11 The solid lines show the observed intensity distributions in the horizontal direction (the dispersion plane) as a function of γ. (a) C IV 1548.2 Å, (b) N V 1238.8 Å and (c) O VI 1031.9 Å emitted from JIPP T-IIU plasma. The dotted lines show the calculated intensity distributions in the horizontal direction.

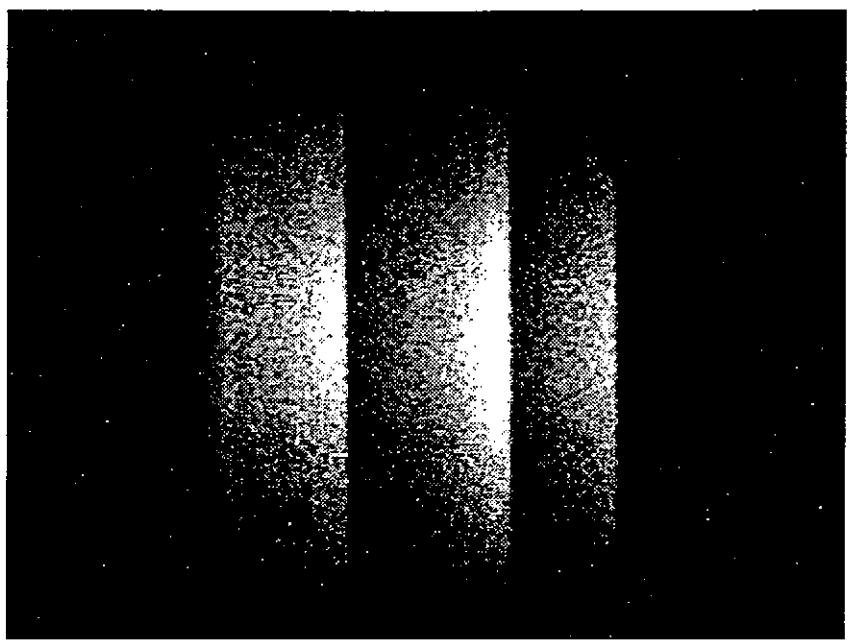

Fig. 5-12 Image from the tripartite grating measured at 1048 Å of Ar I in the TPD-S plasma. The grating used is blazed at 800 Å.

5.3.3 Images of the TPD-S Plasma

In order to see the spatial sensitivity in VUV wavelength, TPD-S is used as a light source. The image at Ar I 1048 Å and the intensity profiles are shown in Fig. 5-13 as a typical example.

As shown in Fig. 5-13, the observed intensity distribution in the plasma column image with the spectral line of Ar I at 1048 Å varies in the horizontal direction, in spite of the homogeneity of the plasma column along the axis. In this measurement, the grating blazed at 1500 Å was used. At the measurements of the spectral lines close to the blaze wavelength, the good uniformity was found in the horizontal direction. For the example, the observation of C IV 1548.2 Å emission distribution with the grating blazed at 1500 Å is shown later in Fig. 6-4.

The non-uniformity of the sensitivity in the horizontal direction may be thought as a problem on the observation of emission distributions. But a calibration procedure is not so complicated one. As shown in Fig. 5-13, the observed relative intensity in the horizontal direction shows itself relative sensitivity, because of the homogeneity of the plasma column along the axis. With using this calibration curve, the observed distribution on O VI 1031.9 Å emission in JIPP T-IIU plasma has been calibrated. As the result, the good uniformity of O VI emission along the toroidal direction has been confirmed within the errors of 10 percent (Fig. 5-14).

By using the homogeneity of the plasma column along the axis, it was shown that the relative sensitivity calibration can be easily attained.

But, in this calibration experiment with the plasma of TPD-S apparatus, available spectral lines for the calibration are quite limited because of a low electron temperature. In Fig. 5-15, relative sensitivities along the horizontal direction are presented for four different wavelengths. Here, C IV 1548.2 Å, C III 977 Å and N V 1238.8 Å spectral line from JIPP T-IIU plasma were used under the assumption of the homogeneous distribution in toroidal direction.

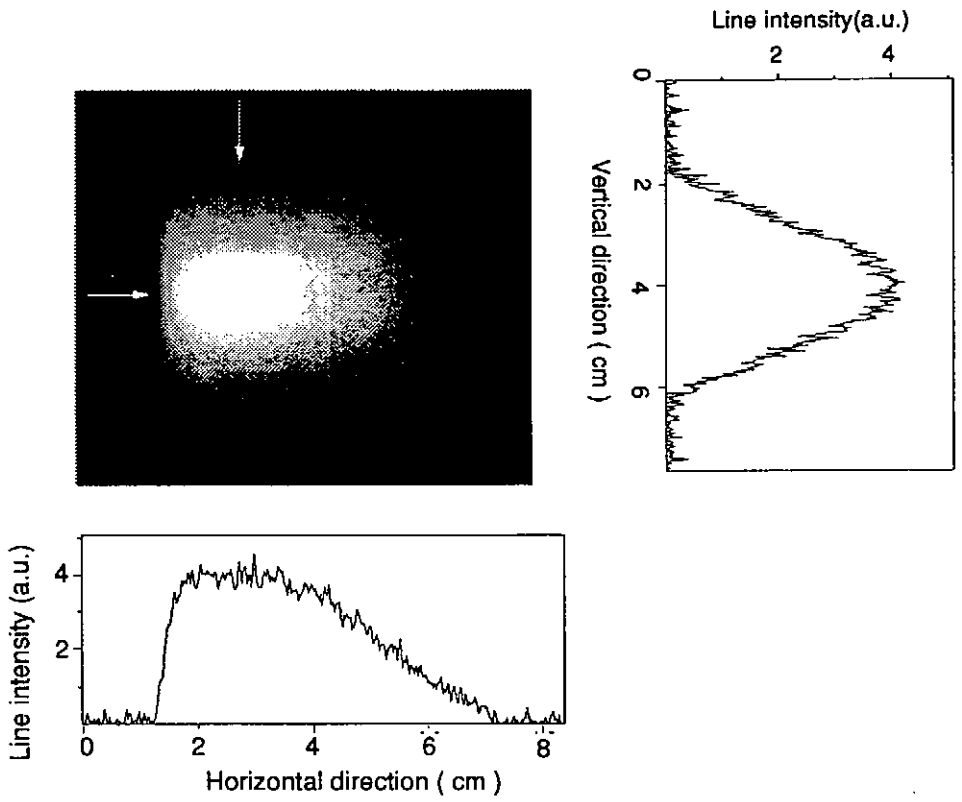

Fig. 5-13 Image and its intensity profiles of the plasma column at 1048 Å for Ar I emission.

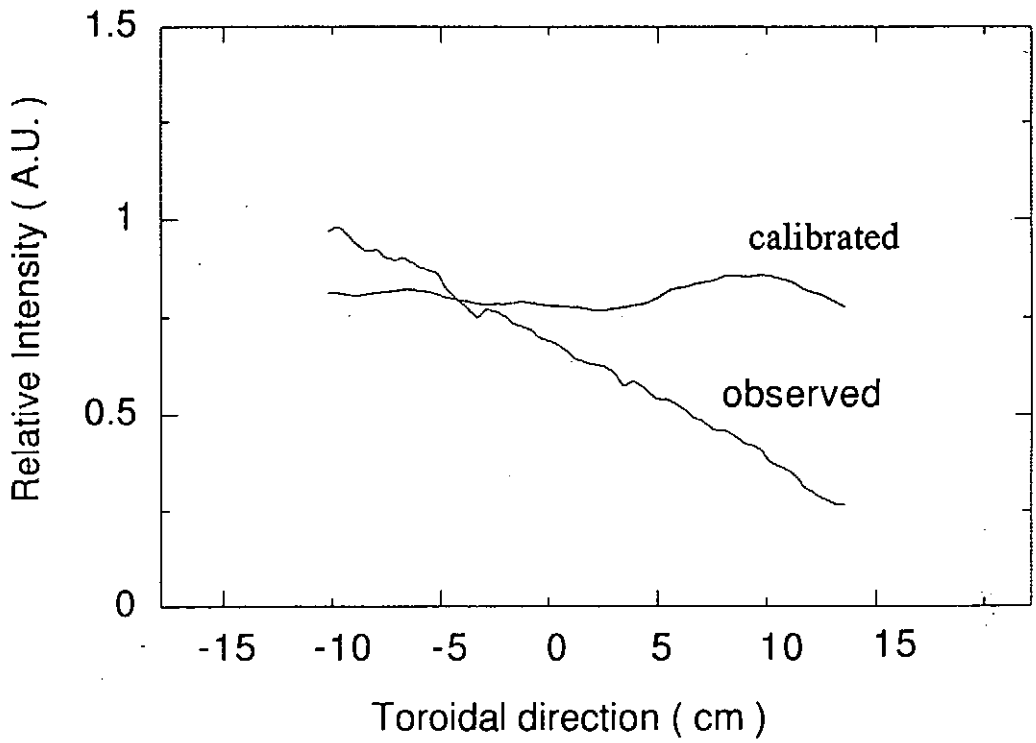

Fig. 5-14 The calibrated intensity distribution of O VI 1031.9 Å emission along the toroidal direction, which is obtained from the measurement of Ar I 1048 Å .

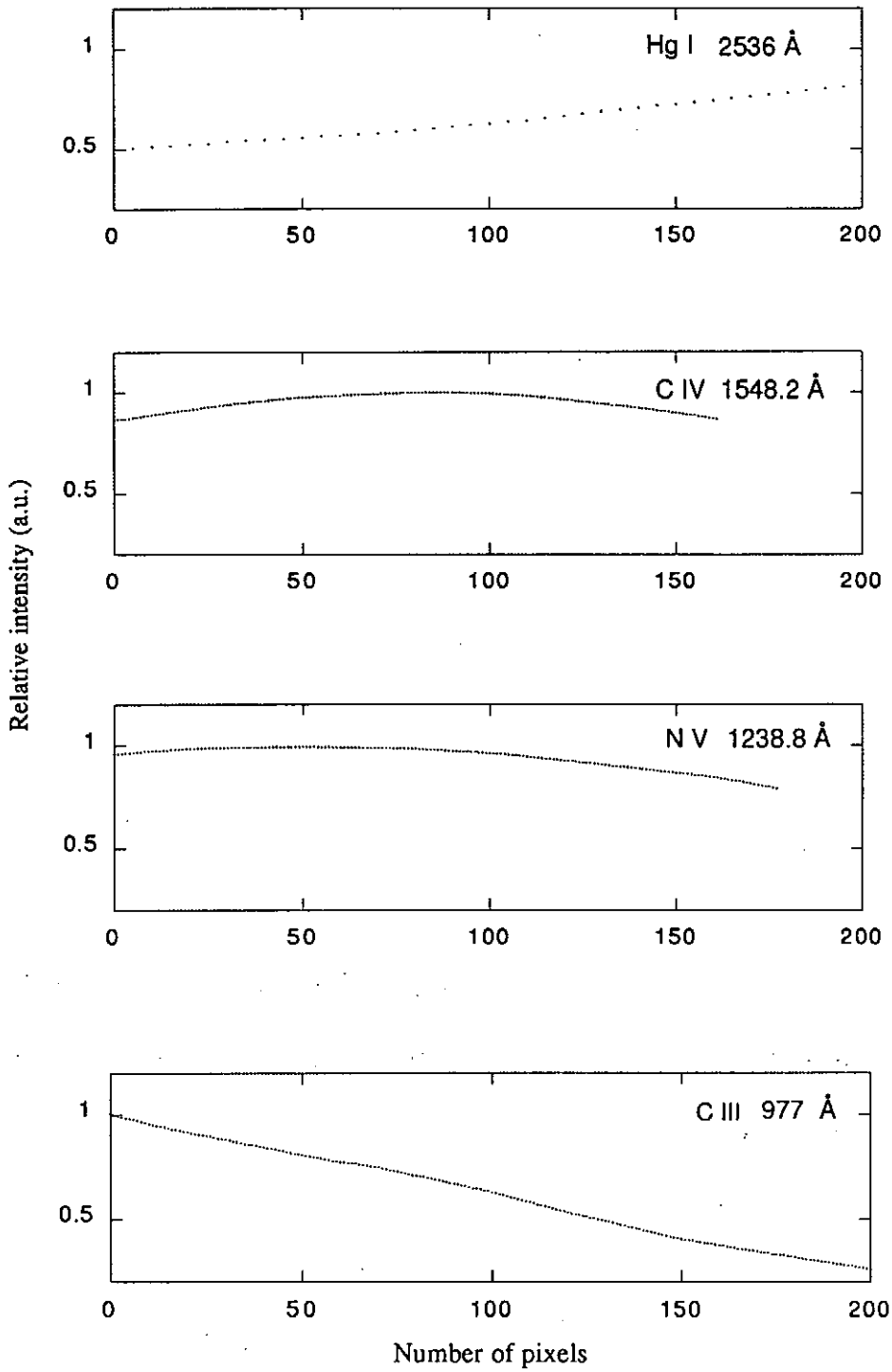

Fig. 5-15 Relative sensitivity curves for various wavelengths.

6. Measurements of Radial Distribution of Impurity Ions in Tokamak Plasma

The usefulness of the imaging system was demonstrated by applying on the measurement of JIPP T-IIU tokamak plasma at National Institute for Fusion Science (NIFS), Japan.[19]

6.1 Outline of the JIPP T-IIU Tokamak

The JIPP T-IIU tokamak is a device which has a major radius of 0.91 m and a minor radius of 0.23 m determined by the fixed carbon limiter (Fig. 6-1). The maximum toroidal field B_t is 3 T and the maximum plasma current I_p is 250 kA with a limiter configuration.

The plasma is heated in the two-ion hybrid heating regime (ion cyclotron range of frequency : ICRF) with a maximum power of 500 kW.[20] Also, a hydrogen beam of 30 keV is injected tangentially (neutral beam injection : NBI), with a maximum input power of 300 kW. ICRF heating and NBI are used as auxiliary heating systems in the present experiment in order to bring the plasma parameters into the proper range.

Device and plasma parameters of the JIPP T-IIU tokamak for limiter and divertor configurations are summarized in Table 6-1.

Time history of a typical shot of the JIPP T-IIU tokamak is shown in Fig. 6-2.

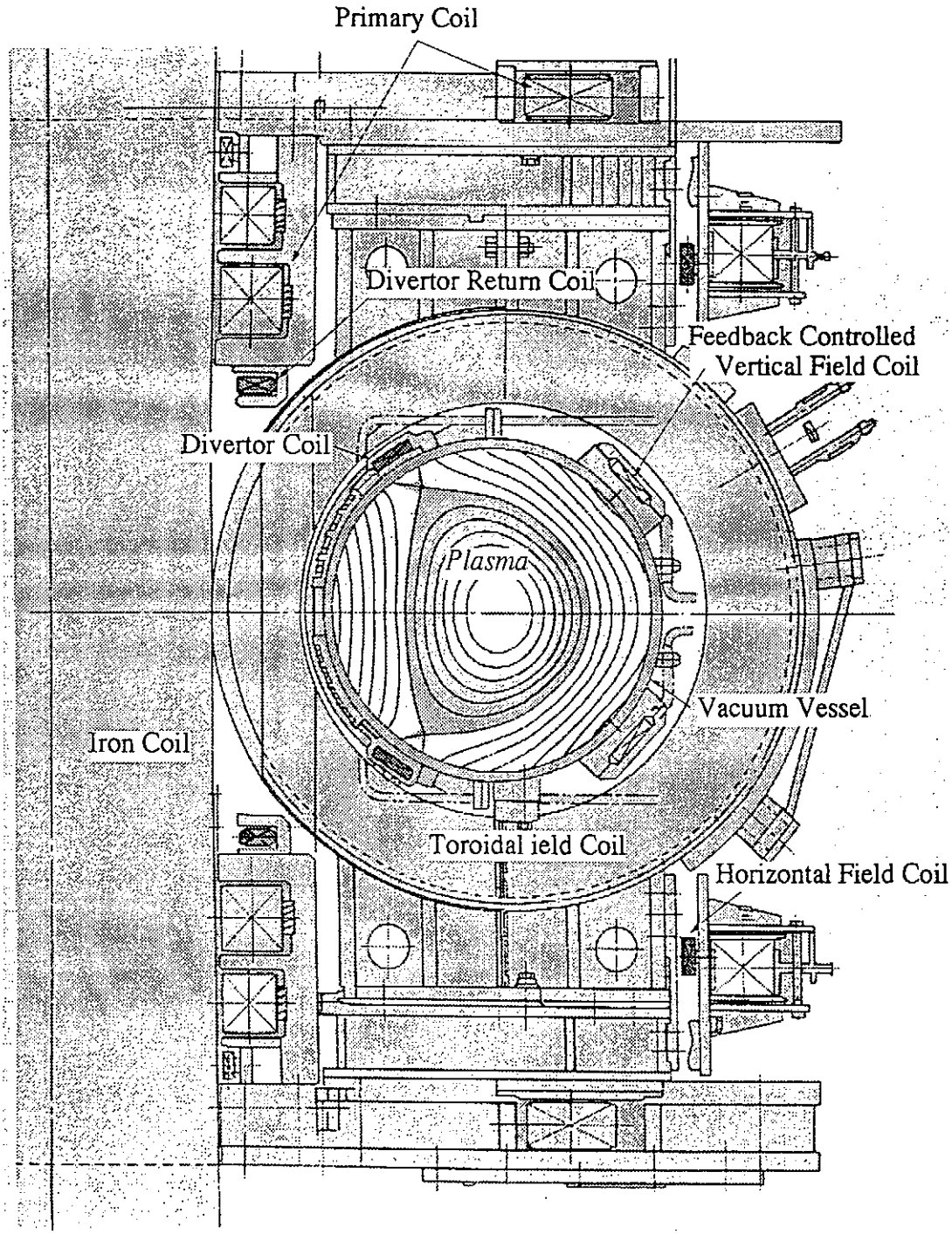

Fig. 6-1 Cross-sectional view of the JIPP T-IIU device.

Table 6-1 Device and plasma parameters of JIPP T-IIU.

	Limiter Configuration
Major Radius	0.89 ~ 0.93 m
Minor Radius	0.21 ~ 0.24 m
Toroidal Field	3 T
Magnetic Flux of Iron Core	~ 1.1 Wb
Plasma Duration	~ 0.5 sec
Plasma Current	200 ~ 320 kA
Plasma Elongation	≤ 1.0
Electron Temperature	~ 1.2 keV (OH)
	~ 2.5 keV (ICRF)
Ion Temperature	~ 0.5 keV (OH)
	~ 2.0 keV (ICRF)
Line-Averaged Electron Density	$\leq 8 \times 10^{13}$ cm^{-3}
Energy Confinement Time	~ 25 ms (OH)
	~ 40 ms (IOC-Mode)
	~ 15 ms (ICRF)
Effective Charge, Zeff	≤ 2
	Divertor Configuration (expected value)
Major Radius	~ 0.91 m
Minor Radius	~ 0.20 m
Toroidal Field	3 T
Magnetic Flux of Iron Core	~ 1.1 Wb
Plasma Duration	~ 0.5 sec
Plasma Current	≤ 150 kA
Plasma Elongation	≤ 1.4

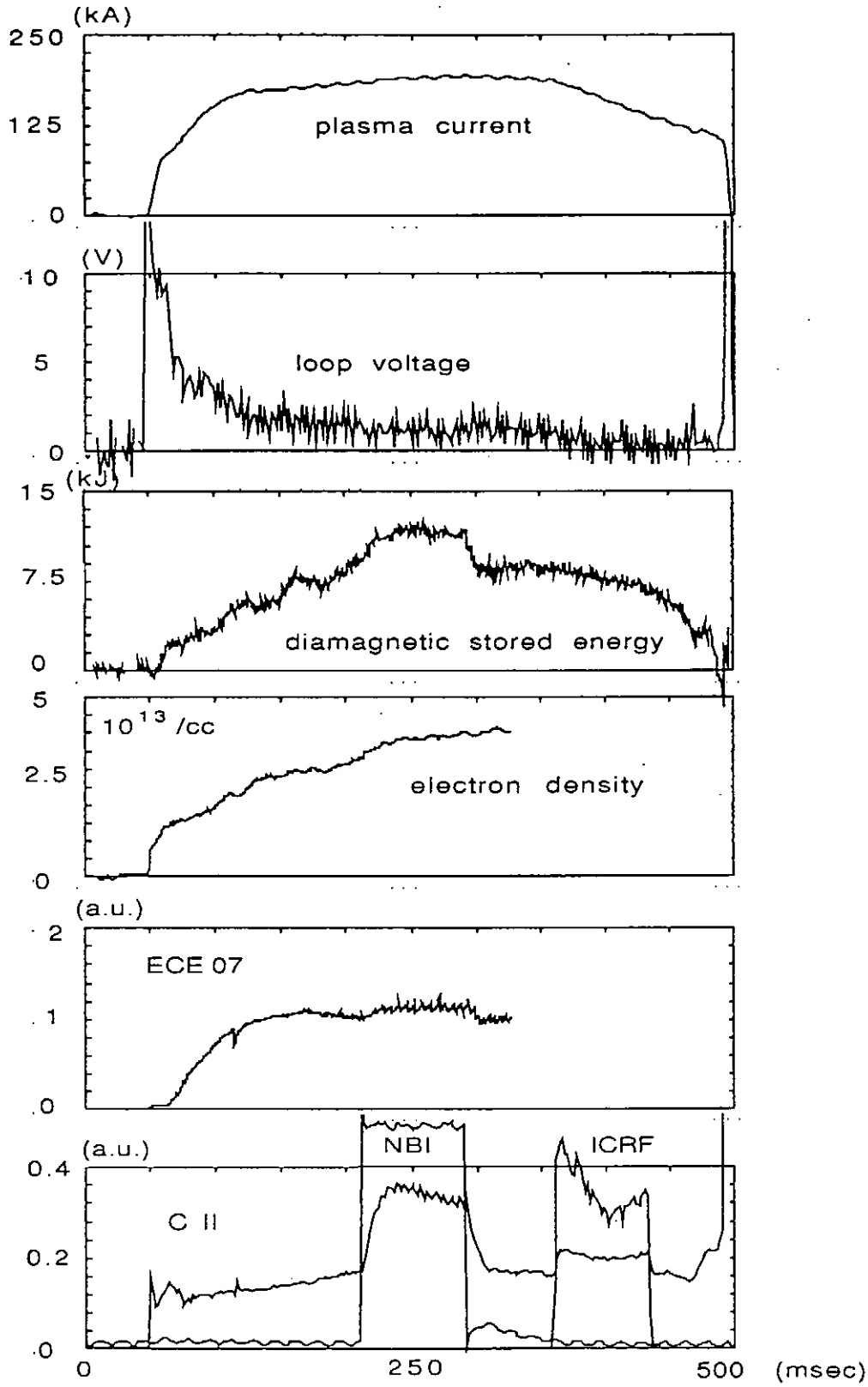

Fig. 6-2 Time evolution of plasma current, loop voltage, diamagnetic stored energy, electron density and temperature at near center, and C II emission in visible wavelength. Heating time of NBI and ICRF is shown.

6.2 Installation of the Imaging System on the JIPP T-IIU Tokamak

The imaging monochromator system has been installed to the JIPP T-IIU tokamak for the observation of spatial distributions of impurity radiation.

The set-up for space-resolved measurements in the vacuum ultraviolet spectral region is shown schematically in Fig. 6-3.

The monochromator-detector system has been mounted at a port of JIPP T-IIU tokamak. This system is positioned at a distance of 4 m from the plasma center to the entrance slit of the monochromator because of the restriction of the space of JIPP T-IIU Lab.

The view area in the plasma is about 38 cm and 22 cm in the horizontal and vertical plane, respectively. This view size in the vertical plane is less than the half of the plasma size (diameter).

The imaging system is inclined below at a degree of 16.4° to view an upper half of the JIPP T-IIU tokamak plasma in the radial direction, which has a limited view area from the plasma center and to a below region of the limiter.

The 6-mm spatial resolution in the vertical direction has been obtained using the entrance slit of 0.15 mm height with a 4-m distance from the entrance slit of the monochromator to the plasma center. The spatial resolution of 3-mm in the horizontal direction has been also achieved.

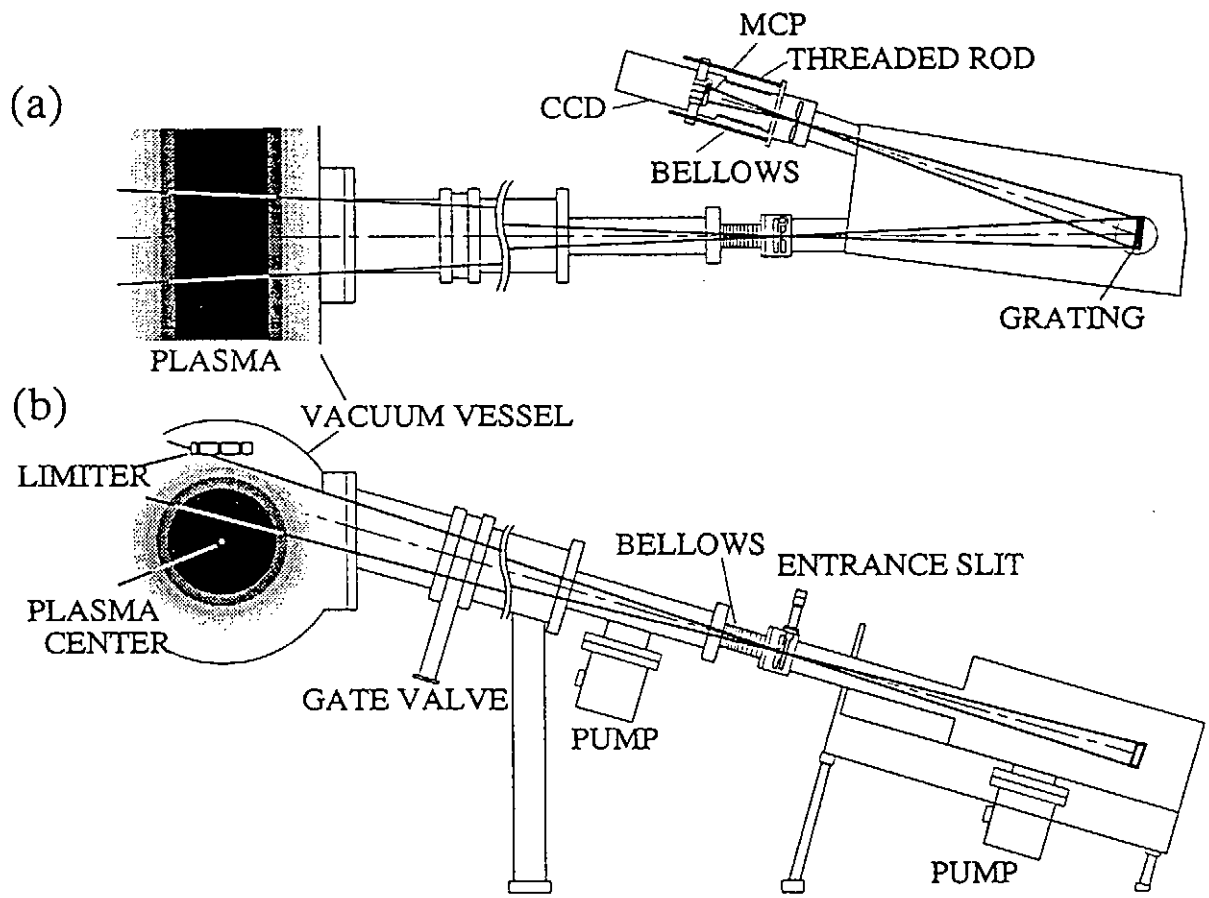

Fig. 6-3 Experimental set up to observe monochromated image from the JIPP T-IIU tokamak. (a) Top view. (b) Vertical view.

6.3 Images and Radial Profiles of Impurity Ions in JIPP T-IIU Plasma

The imaging system was in use on the JIPP T-IIU tokamak. The two-dimensional space-resolved images of the impurity line radiations from a single discharge has been obtained

(a) Image of the impurity line emission

Because of a roughly parabolic radial profiles of electron temperature and electron density, impurity ions in the tokamak plasma localize at certain radial positions according to their ionization stages. Thus, emission lines from impurity ions in certain ionization stages may be expected to have a shell structure.

The typical image of the distribution of C IV $2p\ ^2P_{3/2} \rightarrow 2s\ ^2S_{1/2}$ emission at 1548.2 Å is shown in Fig. 6-4 (a), which is obtained in the discharge with plasma current of 200-kA during ion cyclotron range of frequency (ICRF) heating (200 kW). Its intensity profile is shown in Fig. 6-4 (b).

It shows that C IV ion is concentrated in the radial position of ~20 cm and spreads uniformly in the toroidal direction. The emission of the impurity line is shown as shells near the plasma edge where the electron temperature is of the order of its ionization potential.

The viewing area in the plasma is limited from a 5 centimeter above the plasma center to a slightly below of the limiter radius, which is constrained by the limited grating size and the size of viewing port. The

(a)

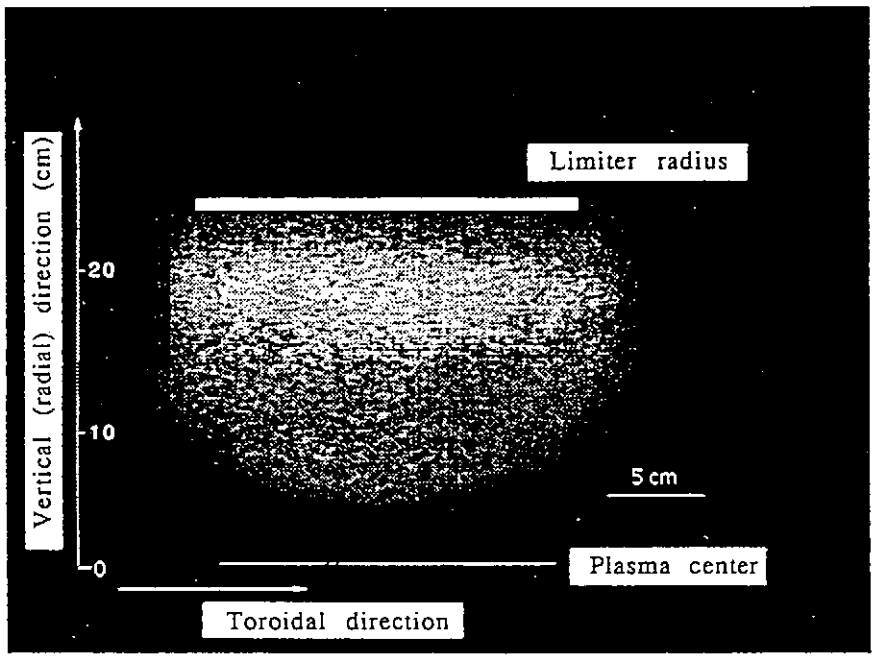

(b)

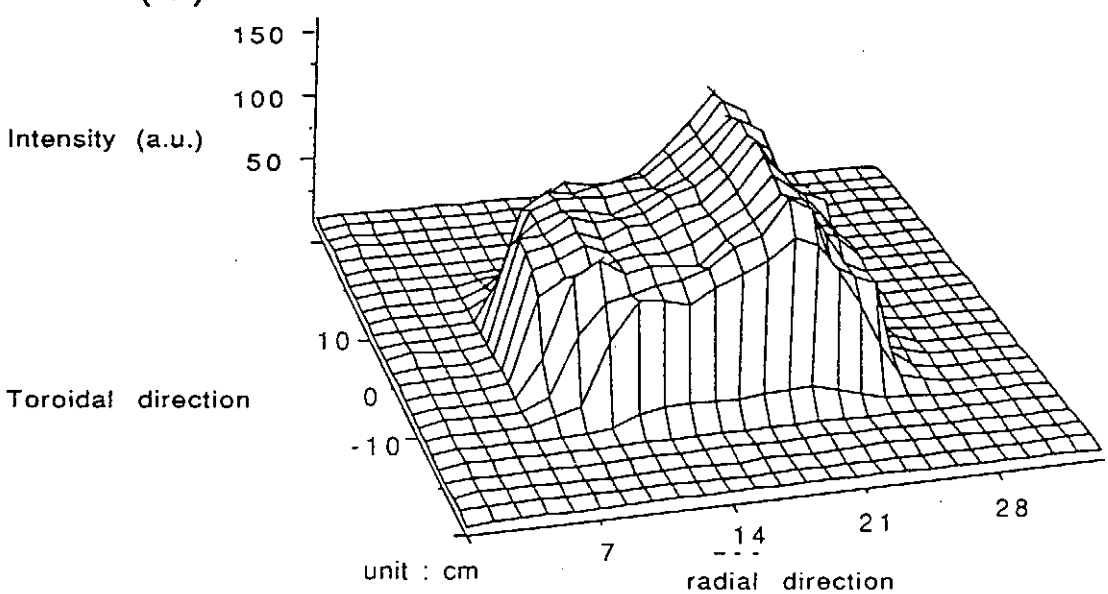

Fig. 6-4 The typical image of C IV emission at 1548.2 Å and viewing area in the JIPP T-IIU tokamak. (a) Observed image. (b) Processed image data which shows the intensity distribution of the spectrum.

images in this work have been obtained with the exposure time of 33 msec.

Result from Fig. 6-4 shows that this imaging system can monitor the 2-D spatially resolved images of the impurity emission line from the tokamak plasma.

(b) Emission profiles of the successive ionization potentials

The difference of the radial distribution which depends on ion species and their ionization stages is shown in Fig. 6-5.

Here, the $2p\,^2P_{3/2} \rightarrow 2s\,^2S_{1/2}$ emission lines of Li-like impurity C IV 1548.2 Å, N V 1238.8 Å and O VI 1031.9 Å have been observed as the example of the distribution with successive ionization potentials (C IV : 64.5 eV, N V : 97.9 eV, O VI : 138.1 eV).

Fig. 6-5 (b) shows a Abel-inverted radial profiles, which are normalized to the peak value. In this processes, the inner tail and the outer increase of the ion density profiles is disregarded due to the poor precision of the Abel-inversion procedure in this region.

The radial positions of the peaks are in the right order taking into account their respective ionization potentials and the decrease of the electron temperature towards the plasma edge.

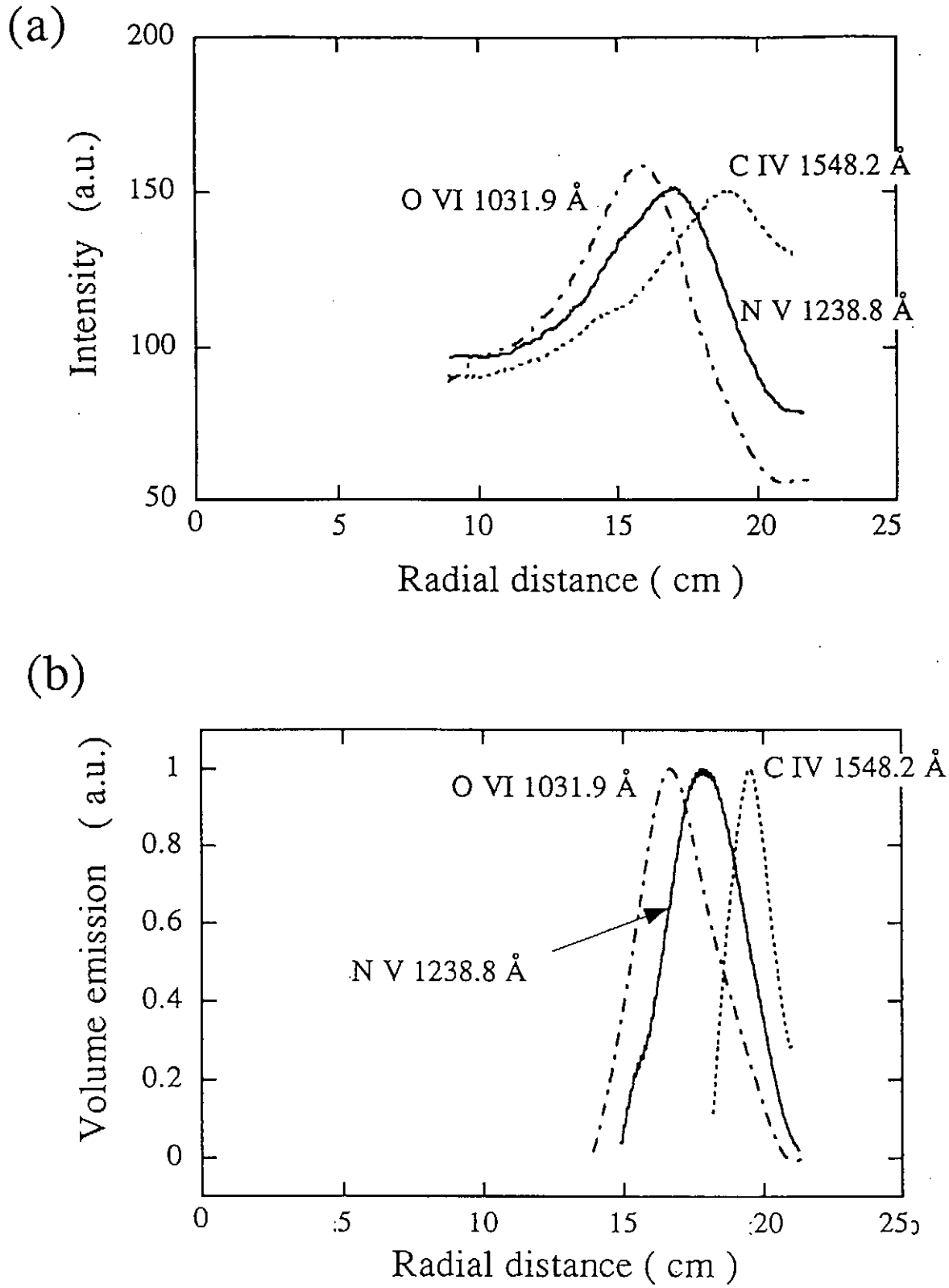

Fig. 6-5 (a) Observed emission profiles of the Li-like ions C IV, N V, and O VI. (b) Abel-inverted radial profiles, which are normalized to the peak value.

(c) Time Evolution of the Radial Profile of the Impurity Ion

Temporal behaviors of the radial distribution have been measured for O VI emission line at 1031.9 Å.

Figure 6-6 shows the evolution of the Abel-inverted radial profiles of the O VI emission line, which has been obtained with the different phase in the discharge; (1) initial buildup phase, (2) current plateau (plasma current of 200 kA), and (3) during the ICRF heating (200 kW). Typical time evolution of the O VI emission line and each phases measured are shown in Fig. 6-7.

It is seen that in the initial buildup phase, oxygen impurity is almost uniformly distributed since the deep penetration of the impurities into the discharge is possible due to the low temperature and density.

However, after this initial ionization phase, the temperature and density rapidly increase and penetration to the center of the incoming flux is no more possible; the emission profile of the ion therefore develops a cylindrical shell structure (Fig. 6-6 (2)). The variation of the emitting shell position corresponds to the evolution of the peripheral electron temperature.

During the ICRF heating, the shell peak of O VI emission shifts to the more outside from the plasma center, compared to the peak at the current plateau phase. This shift may be understandable as the results of the change of radial profiles of electron temperature and density, hence the shell position moves outward as T_e increases.

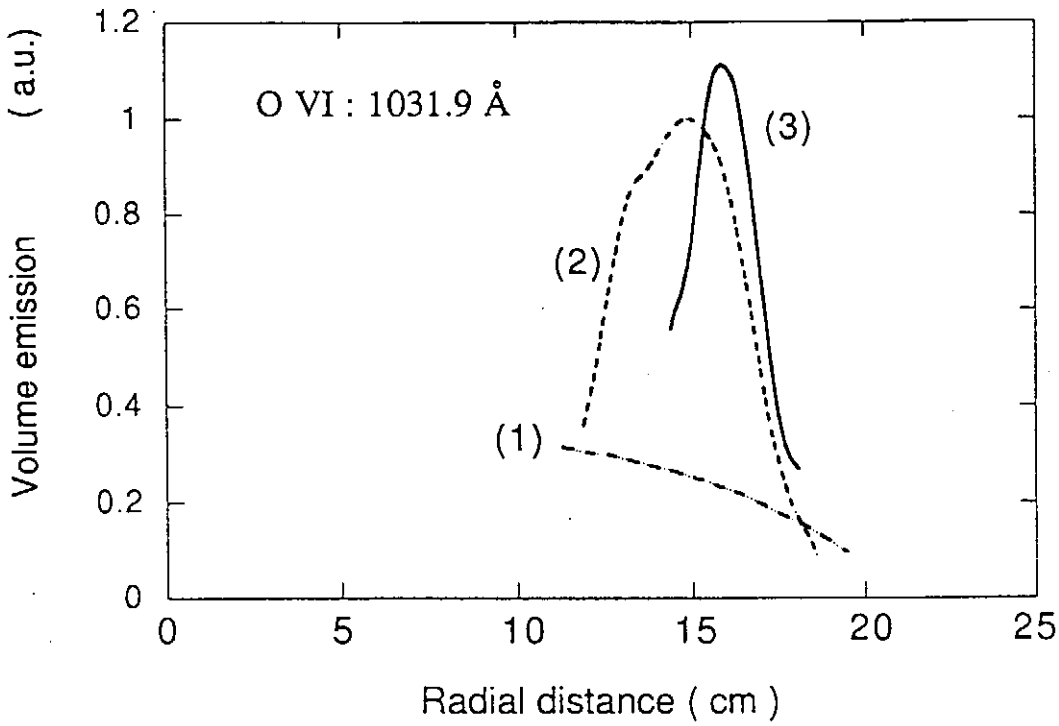

Fig. 6-6 The Abel-inverted radial profiles of the O VI emission.
(1)initial buildup phase, (2) current plateau, (3) during the ICRF heating.

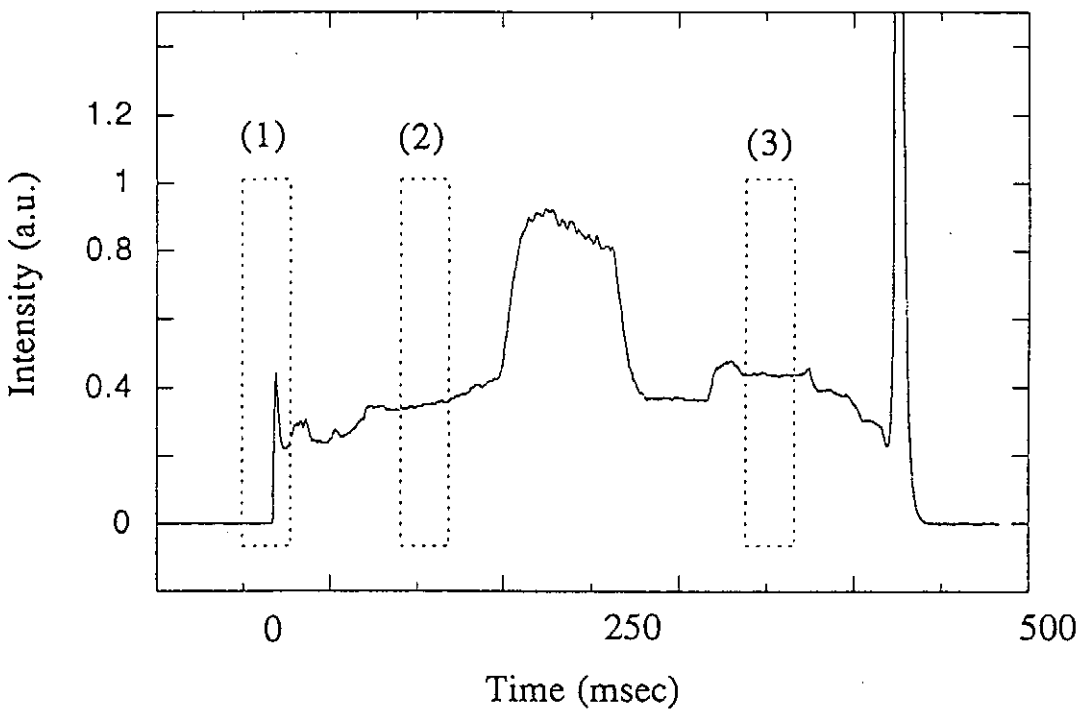

Fig. 6-7 Time history of the O VI emission line and the each phases obtained.

7. Conclusion

A two-dimensional imaging monochromator in normal incidence region (400 Å ~ 2000 Å) was developed, and its performances under various testing conditions were studied.

The imaging is achieved by using the entrance slit of limited height as a pin hole and the 2-D detector system displaced away from the exit slit of the monochromator.

Ray tracing was performed in order to evaluate the imaging properties and to study the effect of aberrations, mainly astigmatism and coma, which is caused by a concave grating.

In order to see the spatial resolution and the relative sensitivity on spatial coverage of the imaging system in vacuum ultraviolet wavelength region, a stationary arc discharge (TPD-S) was developed as a light source. An aperture mask has been settled to measure the spatial resolution of the imaging system. The measured spatial resolution is about 0.5 mrad and 1 mrad in the dispersion and vertical plane, respectively, with the entrance slit of 0.1 mm width and height.

To verify the focusing property in the vertical plane and see the relative sensitivity on a viewing direction, the monochromated image of a mercury lamp was exposed on a photographic film. In the vertical direction, the flat sensitivity was concluded. However, it was found that there is a strong non-uniformity on the sensitivity in the direction of

dispersion plane when the wavelength of the image is far from the blazed wavelength of the equipped grating, which is recognized as an effect of a grating.

The imaging monochromator system has been installed to the JIPP T-IIU tokamak for observation of spatial distributions of impurity radiation. The 2-D spatially resolved images of the impurity emission line was obtained successfully. As an example, it is shown that C IV ion is concentrated in the radial position of ~20 cm and spreads uniformly in the toroidal direction. The differences of the radial distributions which depend on ion species and their ionization stages have been observed on the Li-like impurity C IV 1548.2 Å, N V 1238.8 Å and O VI 1031.9 Å. It can be seen that the ion with higher ionization potential is localized more inside the plasma. Temporal behaviors of the radial distribution have been also measured for O VI emission line at 1031.9 Å. It is seen that in the initial buildup phase, oxygen impurity is almost uniformly distributed. During the ICRF heating, the shell peak of O VI emission shifts to the more outside from the plasma center, compared to the peak at the current plateau phase.

The important features of this scheme are the 2-D imaging which does not require a stigmatic property for focusing and an easy fabrication with minor modification of a commercial normal incidence monochromator. One problem of this instrument may be a non-uniformity of the sensitivity in the direction parallel to the dispersion plane, which originated from a grating. In principle, the non-uniformity problem of the sensitivity in the dispersion plane may be solved with an introduction of a non-blazed holographic grating or a laminar grating.

But it may lose a merit of high reflectivity around the blazed wavelength. The interchangeable grating mount equipped with several gratings with different blazed wavelengths is thought to be useful in practice. By incorporating a multilayer coated grating[21], which can produce high reflectivity at non-grazing angles as Bragg reflectors[22], the imaging system shown here will be applicable even in the extreme-ultraviolet and soft x-ray region.

References.

1. TFR Group, Phys. Rev. Lett. **36**, 1306 (1979).

2. TFR Group, Plasma Phys. **20**, 207 (1978).

3. D. Content, D. Wroblewski, M. Perry, and H. W. Moos, Rev. Sci. Instrum. **57**(8), 2041 (1986).

4. A. Nudelfuden, R. Solanki, and H. W. Moos, Appl. Opt. **31**, 789 (1985).

5. N. Yamaguchi, J. Katoh, Y. Sato, T. Aota, A. Mase, and T. Tamano, Rev. Sci. Instrum. **65**(11), 3408 (1994).

6. R. K. Richards, H. W. Moos, and S. L. Allen, Rev. Sci. Instrum. **51**(1), 1 (1980).

7. J. A. R. Samson, *Techniques of vacuum ultraviolet spectroscopy* (Wiley, New York, 1967).

8. M. C. E. Huber, and G. Tondello, Appl. Opt. **18**, 3948 (1979).

9. G. Tondello, Optica Acta, **26**, 357 (1979).

10. R. J. Fonck, A. T. Ramsey, and R. V. Yelle, Appl. Opt. **21**, 2115 (1982).

11. C. R. Runge and R. Mannkopf, Z. Physik **45**, 13 (1927).

12. H. G. Beutler, J. Opt. Soc. Am. **35**, 311, (1945).

13. T. Namioka, J. Opt. Soc. Am **49**, 446 (1959).

14. T. Namioka, J. Opt. Soc. Am **49**, 460 (1959).

15. T. Namioka, J. Opt. Soc. Am **49**, 951 (1959).

16. T. Namioka, J. Opt. Soc. Am **51**, 4 (1961).

17. B. Lai and F. Cerrina, Nucl. Instrum. and Meth. **A246**, 337 (1986).

18. B. Lai, K. Chapman and F. Cerrina, Nucl. Instrum. and Meth. **A266**, 544 (1988).

19. K. Toi, et al 1991 *Proc. 13th Int. Conf. on Plasma Physics and Controlled Nuclear Fusion Research*(Washington,DC), vol 1 (V ienna:IAEA), p 301.

20. T. Seki, T. Watari, K. Adati, Y. Hamada, K. Ida, K. Itoh, K. Kawahata, S. Morita, K. Narihara, K. Toi, et al, Nuclear Fusion, **31**(7), 1369 (1991)

21. R. J. Thomas, R. A. M. Keski-kuha, W. M. Neupert, C. E. Condor,

and J. S. Gum, Appl. Opt. **30**, 2245 (1991).

22. T. W. Barbee, Jr., Rev. Sci. Instrum. **60**, 1588 (1989).

Recent Issues of NIFS Series

NIFS-376 S. Bazdenkov, T. Sato, K. Watanabe and The Complexity Simulation Group,
Multi-Scale Semi-Ideal Magnetohydrodynamics of a Tokamak Plasma; Sep. 1995

NIFS-377 J. Uramoto,
Extraction of Negative Pionlike Particles from a H2 or D2 Gas Discharge Plasma in Magnetic Field; Sep. 1995

NIFS-378 K. Akaishi,
Theoretical Consideration for the Outgassing Characteristics of an Unbaked Vacuum System; Oct. 1995

NIFS-379 H. Shimazu, S. Machida and M. Tanaka,
Macro-Particle Simulation of Collisionless Parallel Shocks; Oct. 1995

NIFS-380 N. Kondo and Y. Kondoh,
Eigenfunction Spectrum Analysis for Self-organization in Dissipative Solitons; Oct. 1995

NIFS-381 Y. Kondoh, M. Yoshizawa, A. Nakano and T. Yabe,
Self-organization of Two-dimensional Incompressible Viscous Flow in a Friction-free Box; Oct. 1995

NIFS-382 Y.N. Nejoh and H. Sanuki,
The Effects of the Beam and Ion Temperatures on Ion-Acoustic Waves in an Electron Beam-Plasma System; Oct. 1995

NIFS-383 K. Ichiguchi, O. Motojima, K. Yamazaki, N. Nakajima and M. Okamoto
Flexibility of LHD Configuration with Multi-Layer Helical Coils; Nov. 1995

NIFS-384 D. Biskamp, E. Schwarz and J.F. Drake,
Two-dimensional Electron Magnetohydrodynamic Turbulence; Nov. 1995

NIFS-385 H. Kitabata, T. Hayashi, T. Sato and Complexity Simulation Group,
Impulsive Nature in Collisional Driven Reconnection; Nov. 1995

NIFS-386 Y. Katoh, T. Muroga, A. Kohyama, R.E. Stoller, C. Namba and O. Motojima,
Rate Theory Modeling of Defect Evolution under Cascade Damage Conditions:The Influence of Vacancy-type Cascade Remnants and Application to the Defect Production Chracterization by Microstructural Analysis; Nov. 1995

NIFS-387 K. Araki, S. Yanase and J. Mizushima,
Symmetry Breaking by Differential Rotation and Saddle-node Bifurcation of the Thermal Convection in a Spherical Shell; Dec. 1995

NIFS-388 V.D. Pustovitov,
Control of Pfirsch-Schlüter Current by External Poloidal Magnetic Field in Conventional Stellarators: Dec. 1995

NIFS-389 K. Akaishi,
On the Outgassing Rate Versus Time Characteristics in the Pump-down of an Unbaked Vacuum System; Dec. 1995

NIFS-390 K.N. Sato, S. Murakami, N. Nakajima, K. Itoh,
Possibility of Simulation Experiments for Fast Particle Physics in Large Helical Device (LHD); Dec. 1995

NIFS-391 W.X.Wang, M. Okamoto, N. Nakajima, S. Murakami and N. Ohyabu,
A Monte Carlo Simulation Model for the Steady-State Plasma in the Scrape-off Layer; Dec. 1995

NIFS-392 Shao-ping Zhu, R. Horiuchi, T. Sato and The Complexity Simulation Group,
Self-organization Process of a Magnetohydrodynamic Plasma in the Presence of Thermal Conduction; Dec. 1995

NIFS-393 M. Ozaki, T. Sato, R. Horiuchi and the Complexity Simulation Group
Electromagnetic Instability and Anomalous Resistivity in a Magnetic Neutral Sheet; Dec. 1995

NIFS-394 K. Itoh, S.-I Itoh, M. Yagi and A. Fukuyama,
Subcritical Excitation of Plasma Turbulence; Jan. 1996

NIFS-395 H. Sugama and M. Okamoto, W. Horton and M. Wakatani,
Transport Processes and Entropy Production in Toroidal Plasmas with Gyrokinetic Eletromagnetic Turbulence; Jan. 1996

NIFS-396 T. Kato, T. Fujiwara and Y. Hanaoka,
X-ray Spectral Analysis of Yohkoh BCS Data on Sep. 6 1992 Flares - Blue Shift Component and Ion Abundances -; Feb. 1996

NIFS-397 H. Kuramoto, N. Hiraki, S. Moriyama, K. Toi, K. Sato, K. Narihara, A. Ejiri, T. Seki and JIPP T-IIU Group,
Measurement of the Poloidal Magnetic Field Profile with High Time Resolution Zeeman Polarimeter in the JIPP T-IIU Tokamak; Feb. 1996

NIFS-398 J.F. Wang, T. Amano, Y. Ogawa, N. Inoue,
Simulation of Burning Plasma Dynamics in ITER; Feb. 1996

NIFS-399 K. Itoh, S-I. Itoh, A. Fukuyama and M. Yagi,
Theory of Self-Sustained Turbulence in Confined Plasmas; Feb. 1996

NIFS-400 J. Uramoto,
A Detection Method of Negative Pionlike Particles from a H2 Gas

Descharge Plasma; Feb. 1996

NIFS-401 K.Ida, J.Xu, K.N.Sato, H.Sakakita and JIPP TII-U group,
Fast Charge Exchange Spectroscopy Using a Fabry-Perot Spectrometer in the JIPP TII-U Tokamak; Feb. 1996

NIFS-402 T. Amano,
Passive Shut-Down of ITER Plasma by Be Evaporation; Feb. 1996

NIFS-403 K. Orito,
A New Variable Transformation Technique for the Nonlinear Drift Vortex; Feb. 1996

NIFS-404 T. Oike, K. Kitachi, S. Ohdachi, K. Toi, S. Sakakibara, S. Morita, T. Morisaki, H. Suzuki, S. Okamura, K. Matsuoka and CHS group; *Measurement of Magnetic Field Fluctuations near Plasma Edge with Movable Magnetic Probe Array in the CHS Heliotron/Torsatron*; Mar. 1996

NIFS-405 S.K. Guharay, K. Tsumori, M. Hamabe, Y. Takeiri, O. Kaneko, T. Kuroda,
Simple Emittance Measurement of H- Beams from a Large Plasma Source; Mar. 1996

NIFS-406 M. Tanaka and D. Biskamp,
Symmetry-Breaking due to Parallel Electron Motion and Resultant Scaling in Collisionless Magnetic Reconnection; Mar. 1996

NIFS-407 K. Kitachi, T. Oike, S. Ohdachi, K. Toi, R. Akiyama, A. Ejiri, Y. Hamada, H.Kuramoto, K. Narihara, T. Seki and JIPP T-IIU Group,
Measurement of Magnetic Field Fluctuations within Last Closed Flux Surface with Movable Magnetic Probe Array in the JIPP T-IIU Tokamak; Mar. 1996

NIFS-408 K. Hirose, S. Saito and Yoshi.H. Ichikawa
Structure of Period-2 Step-1 Accelerator Island in Area Preserving Maps; Mar. 1996

NIFS-409 G.Y.Yu, M. Okamoto, H. Sanuki, T. Amano,
Effect of Plasma Inertia on Vertical Displacement Instability in Tokamaks; Mar. 1996

NIFS-410 T. Yamagishi,
Solution of Initial Value Problem of Gyro-Kinetic Equation; Mar. 1996

NIFS-411 K. Ida and N. Nakajima,
Comparison of Parallel Viscosity with Neoclassical Theory; Apr. 1996

NIFS-412 T. Ohkawa and H. Ohkawa,
Cuspher, A Combined Confinement System; Apr. 1996

NIFS-413 Y. Nomura, Y.H. Ichikawa and A.T. Filippov,
Stochasticity in the Josephson Map; Apr. 1996

NIFS-414 J. Uramoto,
Production Mechanism of Negative Pionlike Particles in H_2 Gas Discharge Plasma; Apr. 1996

NIFS-415 A. Fujisawa, H. Iguchi, S. Lee, T.P. Crowley, Y. Hamada, S. Hidekuma, M. Kojima,
Active Trajectory Control for a Heavy Ion Beam Probe on the Compact Helical System; May 1996

NIFS-416 M. Iwase, K. Ohkubo, S. Kubo and H. Idei
Band Rejection Filter for Measurement of Electron Cyclotron Emission during Electron Cyclotron Heating; May 1996

NIFS-417 T. Yabe, H. Daido,T. Aoki, E. Matsunaga and K. Arisawa,
Anomalous Crater Formation in Pulsed-Laser-Illuminated Aluminum Slab and Debris Distribution; May 1996

NIFS-418 J. Uramoto,
Extraction of K^- Mesonlike Particles from a D_2 Gas Discharge Plasma in Magnetic Field; May 1996

NIFS-419 J. Xu, K. Toi, H. Kuramoto, A. Nishizawa, J. Fujita, A. Ejiri, K. Narihara, T. Seki, H. Sakakita, K. Kawahata, K. Ida, K. Adachi, R. Akiyama, Y. Hamada, S. Hirokura, Y. Kawasumi, M. Kojima, I. Nomura, S. Ohdachi, K.N. Sato
Measurement of Internal Magnetic Field with Motional Stark Polarimetry in Current Ramp-Up Experiments of JIPP T-IIU; June 1996

NIFS-420 Y.N. Nejoh,
Arbitrary Amplitude Ion-acoustic Waves in a Relativistic Electron-beam Plasma System; July 1996

NIFS-421 K. Kondo, K. Ida, C. Christou, V.Yu.Sergeev, K.V.Khlopenkov, S.Sudo, F. Sano, H. Zushi, T. Mizuuchi, S. Besshou, H. Okada, K. Nagasaki, K. Sakamoto, Y. Kurimoto, H. Funaba, T. Hamada, T. Kinoshita, S. Kado, Y. Kanda, T. Okamoto, M. Wakatani and T. Obiki,
Behavior of Pellet Injected Li Ions into Heliotron E Plasmas; July 1996

NIFS-422 Y. Kondoh, M. Yamaguchi and K. Yokozuka,
Simulations of Toroidal Current Drive without External Magnetic Helicity Injection; July 1996

NIFS-423 Joong-San Koog
Development of an Imaging VUV Monochromator in Normal Incidence Region; July 1996